Efferocytosis of SARS-CoV-2-infected dying cells impairs macrophage anti-inflammatory functions and clearance of apoptotic cells

Ana C. G. Salina[1†], Douglas dos-Santos[1†], Tamara S. Rodrigues[1†], Marlon Fortes-Rocha[1], Edismauro G. Freitas-Filho[1], Daniel L. Alzamora-Terrel[1], Mikhael H. F. de Lima[2], Daniele C. Nascimento[2], Ícaro M. S. Castro[3], Camila M. Silva[2], Juliana E. Toller-Kawahisa[2], Amanda Becerra[1], Samuel Oliveira[1], Diego B. Caetité[2], Leticia Almeida[1,4], Adriene Y. Ishimoto[1], Thais M. Lima[1], Ronaldo B. Martins[1], Flavio Veras[2], Natália B. do Amaral[5], Marcela C. Giannini[5], Letícia P. Bonjorno[5], Maria I. F. Lopes[5], Maira N. Benatti[7], Sabrina S. Batah[7], Rodrigo C. Santana[5], Fernando C. Vilar[5], Maria A. Martins[6], Rodrigo L. Assad[5], Sergio C. L. de Almeida[5], Fabiola R. de Oliveira[5], Eurico Arruda Neto[1], Thiago M. Cunha[2,4], José C. Alves-Filho[2,4], Fernando Q. Cunha[2,4], Alexandre T. Fabro[7], Helder I. Nakaya[3,4], Dario S. Zamboni[1,4], Paulo Louzada-Junior[5], Rene D. R. Oliveira[5], Larissa D. Cunha[1]*

[1]Departamento de Biologia Celular e Molecular e Bioagentes Patogênicos, Faculdade de Medicina de Ribeirão Preto, Universidade de São Paulo, Ribeirão Preto, SP, Brazil.
[2]Departamento de Farmacologia, Faculdade de Medicina de Ribeirão Preto, Universidade de São Paulo, Ribeirão Preto, São Paulo, Brazil.
[3]Departamento de Análises Clínicas e Toxicológicas, Faculdade de Ciências Farmacêuticas, Universidade de São Paulo, Brazil.
[4]Center of Research in Inflammatory Diseases (CRID), Faculdade de Medicina de Ribeirão Preto, Universidade de São Paulo, Ribeirão Preto, São Paulo, Brazil.
[5]Divisão de Imunologia Clinica, Emergência, Doenças Infecciosas e Unidade de Terapia Intensiva, Faculdade de Medicina de Ribeirão Preto, Universidade de São Paulo, Ribeirão Preto, SP, Brazil.
[6]Departamento de Cirurgia e Anatomia, Faculdade de Medicina de Ribeirão Preto, Universidade de São Paulo, Ribeirão Preto, SP, Brazil.
[7]Departamento de Patologia e Medicina Legal, Faculdade de Medicina de Ribeirão Preto, Universidade de São Paulo, Ribeirão Preto, SP, Brazil.

[†] A.C.G.S., D.S., and T.S.R. equally contributed to this work.

* Correspondence: Departamento de Biologia Celular e Molecular e Bioagentes Patogênicos
Faculdade de Medicina de Ribeirão Preto, Universidade de São Paulo
Av. Bandeirantes 3900, Ribeirão Preto, SP 14049-900, Brazil
Tel: +55 16 33153319
larissacunha@usp.br
(ORCID iD: 0000-0002-1290-0263),

Abstract

COVID-19 is a disease of dysfunctional immune responses, but the mechanisms triggering immunopathogenesis are not established. The functional plasticity of macrophages allows this cell type to promote pathogen elimination and inflammation or suppress inflammation and promote tissue remodeling and injury repair. During an infection, the clearance of dead and dying cells, a process named efferocytosis, can modulate the interplay between these contrasting functions. Here, we show that engulfment of SARS-CoV2-infected apoptotic cells (AC) exacerbates inflammatory cytokine production, inhibits the expression of efferocytic receptors, and impairs continual efferocytosis by macrophages. We also provide evidence supporting that monocytes and macrophages from severe COVID-19 patients have compromised efferocytic capacity. Our findings reveal that dysfunctional efferocytosis of SARS-CoV-2-infected cell corpses suppress macrophage anti-inflammation and efficient tissue repair programs and provide mechanistic insights for the excessive production of pro-inflammatory cytokines and accumulation of tissue damage associated with COVID-19 immunopathogenesis.

KEYWORDS: COVID-19, macrophage, macrophage polarization, efferocytosis, hyperinflammation, tissue repair

Introduction

Because of its recent emergence, the pathogenesis of COVID-19 is still poorly defined. Patients with severe disease can progress to pneumonia, development of acute respiratory distress syndrome (ARDS) and respiratory failure, septic shock, and multiorgan dysfunction (Siddiqi and Mehra, 2020). These clinical manifestations of the disease have been associated with a dysregulated host immune response and compromised function of the myeloid compartment, suggesting that hyperinflammation and unresolved tissue damage could both contribute to the pathogenesis of severe COVID-19 (Blanco-Melo et al., 2020; Lucas et al., 2020; Rodrigues et al., 2020; Schulte-Schrepping et al., 2020; Silvin et al., 2020; Valle et al., 2020; Veras et al., 2020).

Macrophages and monocytes promote disease tolerance and resolution of inflammation by sensing pathogen and host-derived pathogenic signals and programming their gene expression toward an anti-inflammatory, pro-resolution, and wound-healing phenotype (Martins et al., 2019). This host-protective programming reduces inflammatory cytokine production by other immune and non-immune cells and promotes the repair of damaged tissue to sustain physiological function and re-establish homeostasis (Murray and Wynn, 2011). During the repair process, the efficient clearance of dying cells prevents further tissue dysfunction caused by uncontrolled cytotoxicity and the release of damage-associated molecular patterns (DAMP). Defects in sensing, ingesting, and degradation of dead and dying cells through efferocytosis cause chronic inflammation and autoimmune diseases (Boada-Romero et al., 2020). In addition to preventing the deleterious effects of secondary necrosis, efferocytosis also couples corpse

88 internalization to other environmental cues (such as local cytokines and metabolites) to
89 temporally and spatially regulate macrophage anti-inflammatory and tissue repair functions (A-
90 Gonzalez et al., 2017; Bosurgi et al., 2017; Perry et al., 2019). While the clearance of apoptotic
91 cells is often associated with alternative macrophage programming, the identity of the dying cell,
92 the type of cell death, and the context of death (either sterile or infectious) can modulate the
93 nature of the macrophage response (Rothlin et al., 2020).
94
95 While infection with SARS-CoV2 induces the recruitment of immune cells to the lungs, their
96 role in host defense and the causes for the dysfunction during disease progression remain elusive.
97 Here, we sought to determine how macrophages operate when responding to dying epithelial
98 cells infected with SARS-CoV-2. We found that the presence of viable SARS-CoV-2 in cell
99 corpses dysregulates macrophage anti-inflammatory responses to the efferocytosis of apoptotic
100 cells, promoting excessive production of inflammatory IL-6 and IL-1β while disrupting the
101 efficient continual clearance of dead cells required for effective tissue repair. We also provide
102 evidence that the expression of efferocytic genes is reduced in macrophages from severe
103 COVID-19 patients and that monocytes from hyperinflammatory patients are also less efficient
104 in the clearance of apoptotic cells. Therefore, SARS-CoV-2 infection and the clearance of
105 infected dying cells disrupt macrophage host-protective functions associated with
106 immunopathological manifestations of COVID-19.
107
108 **Results**
109
110 **Macrophages engulf dying cells carrying viable SARS-CoV-2**

111

112 SARS-CoV-2 infection causes cytopathic effects in human and primate epithelial cells (Chu et
113 al., 2020; Zhu et al., 2020), possibly mediated by activation of multiple cell death pathways
114 (Chan et al., 2020; Shaohua Li et al., 2020; Shufen Li et al., 2020; Mulay et al., 2021; Ren et al.,
115 2020; Zhu et al., 2020) . Notably, inhibition of apoptosis ameliorates cytokine expression and
116 tissue damage in the lungs of SARS-CoV-2-infected mice, indicating that apoptosis in the lungs
117 is pathogenic (Chu et al., 2021). Immunofluorescent labeling of active caspase-3 in lung tissues
118 of deceased COVID-19 patients confirmed the induction of apoptosis in pseudostratified
119 epithelia, type I and II pneumocytes infected with replicant SARS-CoV2 (**Fig. 1A**, and **Fig.**
120 **S1A**). Examination of lung tissues also revealed evidence of macrophages with internalized
121 epithelial cells and SARS-CoV-2, suggesting the uptake of infected epithelial cells by
122 macrophages (**Fig. 1B**). Consistent with previous reports (Chu et al., 2020; Ren et al., 2020; Zhu
123 et al., 2020), infection with SARS-CoV-2 induced apoptosis in immortalized epithelial cell lines
124 (both human lung epithelial Calu-3 and simian kidney epithelial Vero CCL81 cells), as shown by
125 annexin V staining (**Fig 1C** and **Fig. S1B**) and caspase-3 activation (**Fig. 1D**). We performed the
126 Median Tissue Culture Infection Dose (TCID50) assay and found that viral particles obtained
127 from isolated apoptotic Vero and Calu-3 cells induced cytopathic effect to an equivalent extent
128 as those released in the culture supernatants (**Fig. S1C**). Furthermore, we isolated annexin V-
129 labelled apoptotic cells (AC) from SARS-CoV-2-infected cell culture and confirmed that they
130 carry viable viral particles (**Fig. 1E**). Therefore, viable SARS-CoV-2 is retained within infected,
131 apoptotic epithelial cells.

132

133 Exposure of phosphatidylserine (PtdSer) on the outer plasma membrane of cells undergoing
134 regulated cell death (RCD), as observed by annexin V binding to infected dying cells (**Fig. 1B**),
135 is the most ubiquitous signal that triggers their phagocytosis (Fadok et al., 1992; Nagata, 2018).
136 To determine whether phagocytes efficiently engulf SARS-CoV-2-infected apoptotic cells
137 (Cov2-AC), we used flow cytometry to assess their uptake by primary human macrophages and
138 macrophages differentiated from THP-1 monocytes. We observed that macrophages efficiently
139 engulf CoV2-AC, similarly to the uptake of sterile, UV-irradiated apoptotic cells (UV-AC) (**Fig.
140 1F and Fig. 1SD**). Analysis by confocal microscopy and staining for Spike protein confirmed
141 the presence of SARS-CoV-2 in engulfed cell corpses (**Fig. 1G**). Finally, either stimulation with
142 infected or sterile dying cells did not robustly affect macrophages viability up to 24 h post-
143 treatment (**Fig. S1E**).
144
145 These results demonstrate that macrophages engulf cell corpses carrying viable particles of
146 SARS-CoV-2, offering a framework to investigate their effects on macrophage function.
147
148 **Efferocytosis of SARS-CoV-2-infected dying cells impairs macrophage anti-inflammatory
149 function**
150
151 We next addressed the effect of the engulfment of SARS-CoV-2-infected apoptotic cells in
152 macrophages. The uptake of sterile apoptotic cells often promotes macrophage functional
153 polarization toward an anti-inflammatory and tissue repair phenotype (Doran et al., 2020). We
154 first observed that stimulation of primary monocyte-derived macrophages with CoV-2-AC, but
155 not infection with SARS-CoV-2, consistently reduced the expression of genes associated with

156 alternative programming to tissue remodeling and secretion of immune-modulatory mediators
157 such as *CCL18*, *CD206* (also known as *MRC1*), *MMP9*, *PPARγ* and *CD163* (**Fig. 2A**).
158 Furthermore, stimulation with UV-irradiated apoptotic Vero cells (UV-AC) increased both gene
159 (**Fig. 2A**) and protein (**Fig. 2B, Fig. S2A**) expression of the anti-inflammatory marker CD206.
160 However, upregulation of MRC1 at the gene or protein levels did not occur in response to
161 stimulation with CoV2-AC (**Fig. 2A and B**). We obtained similar results in THP1-derived
162 macrophages stimulated with CoV2-AC obtained from either Calu-3 or Vero cells infected with
163 SARS-CoV-2 (**Fig. S2B-D**). Stimulation with the conditioned supernatants of infected dying
164 cells (containing putative DAMP, cytokines produced by epithelial cells, extracellular vesicles,
165 and released virions) or direct infection with SARS-CoV-2 did not induce *MRC1* transcription
166 (**Fig. 2A, Fig. S2B**) or translation (**Fig. 2B, Fig. S2C** and **D**) in macrophages. To determine if
167 viral viability was required to modulate CD206 expression by infected apoptotic cells, isolated
168 CoV2-AC were exposed to UV irradiation for virus inactivation (**Fig. S2E**). Notably,
169 macrophages treated with epithelial AC containing inactivated SARS-CoV-2 exhibited increased
170 CD206 surface expression, similar to that of UV-AC (**Fig. 2C**). This finding suggests that viable
171 SARS-CoV-2 actively represses alternative programming carried in dying cells and is not
172 primarily enforced by the type of cell death caused by the infection. Efferocytosis of sterile UV-
173 AC in the presence of SARS-CoV-2 still induced higher expression of CD206 in macrophages
174 (**Fig. 2D**). Therefore, the suppression of the CD206 response required delivery of viral particles
175 within cell corpses to macrophages.
176
177 Conversely, the uptake of CoV2-AC, but not UV-AC, significantly increased *IL6* expression in
178 monocyte- and THP-1-derived macrophages (**Fig. 2E** and **Fig. S2F**, respectively). The uptake of

179 CoV2-AC also induced robust secretion of inflammatory IL-6 and IL-1β, in both primary (**Fig.**
180 **2F**) and THP-1-derived macrophages (**Fig. S2G** and **H**). Importantly, we did not detect these
181 cytokines in macrophages stimulated with the cell-free conditioned supernatants, and therefore
182 this effect was not due to immune mediators or viral particles released from infected epithelial
183 cells (**Fig. 2F** and **Fig. S2F-H**). Further, the induction of inflammatory cytokines by SARS-CoV-
184 2-loaded corpses required the presence of viable viral particles, as UV-treatment or
185 paraformaldehyde-fixation of isolated CoV2-AC abrogated IL-6 secretion (**Fig. 2G**). Notably,
186 we did not observe robust production of IL-6 in response to dying epithelial cells infected with
187 Coxsackievirus (**Fig. S2I** and **Fig. 2H**). This result suggests that augmented pro-inflammatory
188 cytokine production is not a universal response of macrophages to the uptake of cell corpses
189 infected with positive single-strand viruses.
190
191 To confirm the requirement of recognition and binding of CoV2-AC to promote inflammatory
192 skewing, we stimulated macrophages in the presence of annexin V to mask PtdSer exposed on
193 the surface of the apoptotic cells. In the absence of PtdSer ligation, macrophages did not produce
194 IL-6 in response to CoV2-AC (**Fig. 2I** and **Fig. S2J**). Stimulation of macrophages in the
195 presence of actin depolymerization inducer Cytochalasin D, which allows corpse binding but no
196 internalization, also attenuated IL-6 production (**Fig. 2J**).
197
198 Collectively, these findings support that sensing and engulfment of dying cells carrying viable
199 SARS-CoV-2 switch the anti-inflammatory, resolutive programming in response to efferocytosis
200 toward an inflammatory phenotype. The exacerbated cytokine production observed in response

201 to the efferocytosis of infected cell corpses by macrophages may contribute to the cytokine storm
202 associated with COVID-19 hyperinflammatory syndrome.
203
204 **Efferocytosis of SARS-CoV-2-infected dying cells suppresses continual clearance of**
205 **apoptotic cells**
206
207 Several receptors mediate efferocytosis through recognition of PtdSer on the surface of a dying
208 cell, either by direct binding or through a bridging molecule (Boada-Romero et al., 2020;
209 Penberthy and Ravichandran, 2016). We found that engulfment of CoV2-AC by primary
210 macrophages reduced the transcription of such PtdSer receptors, including the scavenger
211 receptors *CD36* and *SRA-I*, *αVβ5* integrin (*ITGB5*), and T cell immunoglobulin mucin receptor 4
212 (*TIM4*) and MER proto-oncogene tyrosine kinase (*MERTK*) (**Fig. 3A**). In THP-1-macrophages,
213 we also observed reduced expression of *SRA-I, ITGB5,* and *TIM4* receptors in response to
214 infection with SARS-CoV-2 (**Fig. S2K**). Phagocytes can ingest multiple corpses in subsequent
215 rounds of efferocytosis (Miyanishi et al., 2007; Morioka et al., 2018; Park et al., 2011; Yurdagul
216 et al., 2020). Previous *in vivo* work showed that macrophages must continually remove ACs to
217 promote efficient repair of injury and prevent the accumulation of secondarily necrotic cells
218 (Wang et al., 2017; Yurdagul et al., 2020). To determine if repression of efferocytic receptors
219 affects additional uptake of dying cells, we treated macrophages with CoV2-AC and
220 subsequently fed them with apoptotic human Jurkat cells (Jurkat-AC). We found that the
221 engulfment of SARS-CoV-2-infected corpses suppressed the efferocytosis of other apoptotic
222 cells (**Fig. 3B-D, Fig. S2L**). As infection with SARS-CoV-2 reduced the expression of some
223 efferocytic receptors in THP-1 macrophages (**Fig. S2K**), we also tested if it affected the uptake

224 of apoptotic cells. Comparatively, infection with SARS-CoV-2 reduced AC clearance to a lower
225 extent than prior uptake of CoV2-AC (**Fig. S2M**). Thus, efferocytosis of SARS-CoV-2-infected
226 dying cells affects the expression of efferocytic receptors and impairs the continual removal of
227 apoptotic cells by macrophages.
228
229 **Lung monocytes and macrophages of severe COVID-19 patients express reduced levels of**
230 **efferocytic receptors**
231
232 To gain insight into the contribution of dysfunctional efferocytosis in COVID-19 pathogenesis,
233 we assessed the expression of efferocytic receptors by immunofluorescence in lung tissues
234 obtained from autopsies of deceased COVID-19 patients. We found a reduction in the protein
235 levels of CD36 in S1009^{+} infiltrating phagocytes in the lungs of COVID-19 patients compared to
236 control tissues (**Fig. 4A**). Phagocytes in the lungs of COVID-19 patients also expressed lower
237 protein levels of MERTK (**Fig. 4B**).
238
239 Using publicly available single-cell RNA sequencing (scRNA-seq) data from bronchoalveolar
240 lavage (BAL)(Liao et al., 2020), we performed enrichment analysis using the genes differentially
241 expressed (DEG) in mild and severe COVID-19 patients compared with healthy individuals. We
242 targeted efferocytosis-related gene ontology annotated pathways and customized gene sets based
243 on the literature (Boada-Romero et al., 2020; Penberthy and Ravichandran, 2016) (**Table S1**).
244 Clusters identified as macrophages (Liao et al., 2020) revealed significant repression of gene sets
245 related to efferocytosis in severe patients (**Fig. 4C**). While differences in the comparison
246 between moderate and severe patients were observed in clusters of early infiltrating phagocytes

247 (S1009^{+} CCL18^{-}), they were more pronounced in mature, putative anti-inflammatory
248 macrophages (S11009^{-} CCL18^{+}). Notably, reassessment on scRNAseq by Ren et al. (2021)
249 showed enrichment in pathways related to efferocytosis for genes repressed in alveolar
250 macrophages which were positive for SARS-CoV-2 RNA compared with those which were
251 negative to the virus (**Fig. 4D**). This finding is consistent with the notion that uptake of infected
252 cells reduces the capacity of macrophages to clear other dead cells. Altogether, these data
253 support that macrophages in the lungs of severe COVID-19 patients may also fail in their
254 efferocytic capacity.
255
256 **Efferocytosis is impaired in monocytes from hyperinflammatory COVID-19 patients**
257
258 Because inflammatory mediators can reduce the expression of efferocytic receptors and the
259 uptake of apoptotic cells (Banerjee et al., 2010; Feng et al., 2011; Michlewska et al., 2008;
260 Olagnier et al., 2011; Thorp et al., 2011), we also investigated if COVID-19 manifestation in the
261 efferocytic potential of blood monocytes. We profiled the monocyte population in blood samples
262 from 26 moderate to severe patients on the day of hospitalization (**Table S2**). Assessment of
263 circulating cytokines confirmed higher IL-6, IL-8, IL-10, and IL-1β in this cohort of patients
264 (**Fig. S3A**)(Lucas et al., 2020; Rodrigues et al., 2020). We observed an increase in the absolute
265 numbers of circulating monocytes and the proportion of monocytes among total leukocytes in
266 COVID-19 patients when compared to healthy control (HC) volunteers (**Fig. S3C-D**), as
267 described (Lucas et al., 2020). These cells also expressed less human leukocyte antigen DR
268 isotype (HLA-DR) on their surface (**Fig. S3D**), as described (Lucas et al., 2020; Schulte-
269 Schrepping et al., 2020). We observed changes in monocytes subsets in COVID-19 patients, with

270 an increase in the percentage of intermediate, inflammatory monocytes ($CD14^{hi}$ $CD16^{+}$) and a
271 reduction in non-classical, anti-inflammatory monocytes ($CD14^{low}$ $CD16^{+}$) that execute
272 efferocytosis more efficiently (**Fig. S3F-H**), similar to other observations (Hamers et al., 2019;
273 Schulte-Schrepping et al., 2020; Silvin et al., 2020). We then assessed the expression of CD36, a
274 lipid-binding receptor with an affinity for anionic phospholipids such as PtdSer exposed on
275 dying cells (Parks et al., 2013; Tait and Smith, 1999), and found reduced surface expression on
276 $CD14^{+}$ monocytes of COVID-19 patients, compared to healthy controls (**Fig. S3I**).
277
278 We next recovered the PBMC blood fraction from 42 COVID-19 patients by density gradient
279 separation and evaluated the expression of efferocytic receptors by qPCR (**Tables S2**). We found
280 a reduced transcription of *CD36*, *SRA-I*, *ITGB5,* and *TIMD4*, but not *MERTK*, in PBMC from
281 COVID-19 patients compared to HC (**Fig. 4E**). Importantly, such a pattern was not observed in
282 PMBC isolated from the blood of patients with acute respiratory distress syndrome unrelated to
283 COVID-19 (**Table S3**) and admitted to the same hospital facility at the time of this study (**Fig.**
284 **4F**). We then addressed a possible association between the levels of efferocytic receptors (**Fig.**
285 **4E**) and the worsening of COVID-19. To that end, we stratified these COVID-19 patients
286 according to their hyperinflammatory state at hospital admission, based on a score of clinical
287 criteria (fever, macrophage activation, hematological dysfunction, coagulopathy, hepatic injury,
288 and cytokinaemia) that defines COVID-19-associated hyperinflammation (cHIS score) (Webb et
289 al., 2020). We found a statistically significant reduction in the expression of *CD36*, *TIMD4,* and
290 *SRA-I* for patients with a cHIS score of at least 2, which is associated with worsening in severity
291 and risk of death (Webb et al., 2020) (**Fig. 4G**).
292

293 Finally, we assessed the uptake of dying cells by monocytes from COVID-19 patients. We
294 stimulated monocytes obtained from PBMC samples from COVID-19 patients with apoptotic
295 cells and evaluated their phagocytic activity by epifluorescence microscopy. We found that
296 monocytes from COVID-19 patients with cHIS score > 2 were less efficient in the uptake of
297 dying cells (**Fig. 4H**). This failure was not caused by an intrinsic defect in phagocytosis, as
298 monocytes from HC and COVID-19 patients internalized zymosan similarly (**Fig. S3J**).
299
300 Thus, monocytes from severe COVID-19 patients that develop hyperinflammation express lower
301 levels of efferocytic receptors and are less efficient in the clearance of dying cells.
302
303 **Discussion**
304
305 In summary, we demonstrate that the sensing and engulfment of SARS-CoV-2-infected dying
306 cells by macrophages switches the effector response to efferocytosis from a potential wound
307 healing, anti-inflammatory function to a pro-inflammatory one. Our data supports that the uptake
308 of cell corpses infected with SARS-CoV-2 exacerbates the secretion of inflammatory IL-6 and
309 IL-1β, suggesting a mechanism for the robust secretion of cytokines related to COVID-19
310 cytokine storm. Another important consequence of this shift in macrophage function is the
311 impairment of macrophage capacity to engulf apoptotic cells continually and promote proper
312 injury resolution. Instead, our data suggest that efferocytosis of infected cells may augment
313 tissue damage by causing inefficient clearance of dead cells. This process may consequently
314 contribute to respiratory complications developed by patients with the severe form of the disease
315 and increase susceptibility to secondary bacterial infections for the lack of effective disease

316 tolerance mechanisms that restrain collateral tissue damage (Jamieson et al., 2013). While such
317 causal connection remains to be investigated, our histological assessment and reanalysis of
318 scRNAseq datasets suggest that the efferocytic capacity of lung macrophages is impaired in the
319 lungs of COVID-19 patients. We further demonstrate that circulating monocytes of COVID-19
320 patients with hyperinflammation present reduced expression of efferocytic receptors and fail to
321 uptake dying cells. While our data is suggestive of a loop between dysfunctional macrophage
322 responses upon the uptake of infected cell corpses in the lungs and signaling affecting efferocytic
323 capacity of blood monocytes, follow-up studies are necessary to establish how COVID-19-
324 associated hyperinflammation impairs the efferocytic machinery in circulating cells. Still,
325 macrophage function in tissue repair and remodeling should be further compromised by the loss
326 of efferocytic potential in infiltrating monocytes.
327
328 In the context of COVID-19 immunopathogenesis, excessive amounts of necrotic cells may lead
329 to high levels of circulating DAMP, such as HMGB1 and lactate dehydrogenase (LDH), both of
330 which correlate with disease severity (Chen et al., 2020; Han et al., 2020; Rodrigues et al., 2020).
331 It is thus possible that the combination of exacerbated cytokine production and interruption of
332 continual efferocytosis in response to engulfment of SARS-CoV-2-infected corpses could both
333 increase the magnitude and duration of inflammation, contributing to the hyperinflammatory
334 state and multiorgan damage in COVID-19. Finally, recent studies reported higher levels of
335 autoantibodies (such as against IFNγ, phospholipids, and annexin A2) in COVID-19 patients
336 (Bastard et al., 2020; Zuniga et al., 2021; Zuo et al., 2020), suggesting that autoantibodies may
337 drive the worsening of the disease. It has long been known that defective engulfment or
338 processing of dying cells causes the development of autoimmune diseases (Boada-Romero et al.,

339 2020; Cohen et al., 2002; Miyanishi et al., 2007; Peng and Elkon, 2011; Rodriguez-Manzanet et
340 al., 2010). In light of our findings, perhaps defective clearance of apoptotic cells caused by
341 SARS-CoV-2 infection and SARS-CoV-2-loaded ACs also contributes to COVID-19-associated
342 autoimmunity.
343
344 As it becomes clear that COVID-19 is a disease of immune dysfunction (Cohen et al., 2002),
345 antivirals, and other therapeutic efforts to limit viral replication may fail to benefit critically ill
346 patients. In those patients, successful therapeutic strategies may rely on targeting dysregulated
347 components of the host response to limit damage to the host, thus promoting disease tolerance
348 and stimulating a resolutive response that restores homeostasis. In this context, our study
349 provides important insights into the mechanisms driving the pathophysiology of COVID-19 that
350 can be explored in the design of therapeutics approaches toward harnessing innate immune
351 responses and macrophage function during SARS-CoV-2 infection.
352
353 **Material and Methods**

354 **Study approval.** The procedures followed in the study were approved by the Research Ethics
355 Committee of Hospital das Clínicas de Ribeirão Preto (CEP-FMRP/USP) and by the National
356 Ethics Committee, Brazil (Comissão Nacional de Ética em Pesquisa (CONEP), protocols
357 30248420.9.0000.5440 and 39722020.9.0000.5440. Written informed consent was obtained from
358 recruited patients.
359
360 **Patient samples.** A total of 59 patients with COVID-19 and 10 patients with non-COVID-19
361 acute respiratory distress syndrome admitted in the Hospital das Clínicas de Ribeirão Preto from

362 April to August 2020 were enrolled in this study. SARS-CoV-2 infection was confirmed by RT-
363 PCR of swab samples, as previously described (Corman et al., 2020). Patients were classified
364 according to their clinical manifestations in (1) mild cases, in which there were mild clinical
365 symptoms and no pneumonia was found in imaging; (2) moderate cases, characterized by fever,
366 respiratory tract symptoms, and pneumonia identifiable by imaging; and (3) severe cases,
367 meaning adults who met any of the following features: arterial partial pressure of oxygen
368 (PaO_2)/oxygen concentration (FiO_2) <300 mm Hg, oxygen saturations at 93% at a rest state and
369 respiratory rate > 30 breaths/min. **Table S2** describes clinical, laboratory, and treatment records
370 of COVID-19 patients. **Table S3** describes clinical, laboratory, and treatment records of non-
371 COVID-19 patients admitted with acute respiratory distress syndrome. Samples from healthy
372 donors tested negative for COVID-19 using RT-PCR or tested negative using serology (specific
373 IgM and IgG antibodies; Asan Easy Test COVID-19 IgM/IgG kits, Asan Pharmaceutical Co.)
374 were used as controls or for isolation of monocytes for in vitro studies.
375
376 **Isolation of human peripheral blood mononuclear cells, monocyte seeding, and**
377 **macrophage differentiation.** Peripheral blood mononuclear cells (PBMC) from healthy donors
378 and COVID-19 patients were isolated from peripheral blood collected in tubes containing EDTA
379 (BD Vacutainer, BD Biosciences). The samples were centrifuged at 400 *g* for 10 min at room
380 temperature (RT), the plasma was discarded, and the cellular portion was diluted in phosphate-
381 buffered saline (PBS). PBMC were isolated by density–gradient centrifugation using
382 Histopaque-1077 (Sigma-Aldrich). The collected PBMC fraction was treated with ACK lysis
383 buffer to lyse erythrocytes and washed twice with PBS. For qRT-PCR, cell lysis proceeded as
384 described below. To obtain monocyte cultures, PBMC were plated on 24-well plates for 1h in

385 serum-free RPMI 1640 (GIBCO) at 37°C in a 5% CO_2 atmosphere for monocyte adhesion. The
386 cells were then washed three times with PBS, followed by media replenishment with RPMI1640
387 media supplemented with penicillin (10.000 U/mL, GIBCO), streptomycin (10.000 µg/mL,
388 GIBCO), 1% glutamine (GIBCO), and 10% heat-inactivated human serum (Sigma Aldrich). For
389 macrophages differentiation, monocytes were cultivated for 7 d in RPMI 1640 supplemented
390 with human serum.
391
392 **Cell Lines.** Calu-3, Vero CCL81, Jurkat, and THP-1 cells were from (ATCC®). Calu-3 and Vero
393 CCL81 cells were maintained in DMEM with 4.5 g/L glucose (GIBCO) supplemented with
394 penicillin (10.000 U/mL), streptomycin (10.000 µg/mL), and 10% heat-inactivated fetal bovine
395 serum (FBS, GIBCO) (DMEMc) at 37°C in a 5% CO_2 atmosphere. Jurkat cells and THP-1 cells
396 were maintained in RPMI1640 media supplemented with penicillin (10.000 U/mL), streptomycin
397 (10.000 µg/mL), 1% glutamine, and 10% FBS (RPMIc) at 37°C in a 5% CO_2 atmosphere.
398
399 THP-1-derived macrophages were obtained by treatment with phorbol 12-myristate 13-acetate
400 (PMA, 50 ng/mL, Sigma-Aldrich) for 24 h, followed by media replenishment with fresh RPMIc
401 and other 24 h incubation period before stimulation.
402 Cell lines were routinely screened for mycoplasma contamination, and all cell lines tested
403 negative.
404
405 **Viral stock.** The SARS-CoV-2 strain (Brazil/SPBR-02/2020) was isolated from the first
406 Brazilian case of COVID-19. The viral stock was produced in a monolayer of Vero CCL81 cells
407 maintained in serum-free DMEM at 37°C in a 5% CO_2 atmosphere. Coxsackievirus B5

408 (Coxsackie) was originally shared by Dr. Roger M. Loria (Virginia Commonwealth University,
409 Richmond, Virginia, USA) (Gomes et al., 2009). The viral stock was produced in a monolayer of
410 HeLa cells maintained in DMEM supplemented with 2% FBS at 37°C and 5% CO_2. Viral stocks
411 were propagated under BSL3 conditions and stored at -80°C. Viral loads were estimated by
412 titration in Vero CCL81 cells seeded onto 96-well plates and standard limiting dilution to
413 confirm the 50% tissue culture infectious dose.
414
415 **Isolation of apoptotic cells.** To generate SARS-CoV-2-infected apoptotic cells (CoV2-AC)
416 from Vero CCL81 and Calu-3 cultures, or Coxsackievirus B5-infected apoptotic cells
417 (Coxsackie-AC) from Vero CCL81 cultures, cell monolayers were rinsed with PBS, replenished
418 with a thin layer of serum-free media, and infection with a freshly thawed virus aliquot at a
419 multiplicity of infection (MOI) of approximately 0.05 was carried out for 1 h at 37°C and 5%
420 CO_2 for viral adsorption. The cells were then topped with fresh media and incubated for 48 h.
421 Sterile apoptotic cells (UV-AC) were generated by exposure to UV-C radiation (Calu-3 cells at
422 500 mJ/cm^2 and Vero CCL81 cells at 350 mJ/cm^2) in a UV crosslinker (Fisher Scientific),
423 followed by 6h incubation in DMEMc at 37°C and 5% CO_2. At the established time points, the
424 supernatants were collected and temporarily stored for further processing. Then, a suspension
425 containing CoV2-AC or UV-AC was obtained by carefully pipetting fresh media up and down
426 the plate surface and collecting loosely attached cells. Following spun at 300 *g* for 5 min,
427 pelleted AC were washed with PBS, resuspended in fresh media, and counted with a Neubauer
428 chamber prior to incubation with macrophages.
429

430 For virus inactivation, isolated AC suspension was placed onto tissue culture hood surface with
431 an open lid for 20 min with the UV-C lamp on. Virus inactivation was confirmed by $TCID_{50}$, as
432 described below. Alternatively, isolated AC were fixed with 2% paraformaldehyde (PFA) in PBS
433 for 10 min and washed twice with PBS before adding to macrophage cultures.
434
435 To prepare the cell-free conditioned supernatants of the infected AC (CoV2-AC Sup), collected
436 supernatants were spun at 300 *g* for 5 min to remove cellular debris; the resulting supernatant
437 was filtered using a 0.22 μm syringe filter and immediately used for macrophage stimulation.
438 The volume of CoV2-AC Sup used to stimulate macrophages was normalized to the amount of
439 collected AC.
440
441 **Cell death assays**. Cells were collected 48 hours post-infection or 6 hours post-irradiation, spun
442 at 300 *g* for 5 min, washed with PBS, and resuspended in the appropriate buffer before labeling.
443
444 Detection of PtdSer was performed by annexin-V labeling (APC annexin-V, BD Biosciences,
445 1:100). 10^6 cells were resuspended in annexin V binding buffer (0.01M HEPES, 0.14M NaCl,
446 2.5 mM CaCl2, pH 7.4), and labeling was carried out for 15 min on ice. The cells were then
447 fixed with 2% PFA in binding buffer for 10 min and washed before flow cytometric analyses.
448
449 For the analysis of cleaved caspase-3, infection of Calu-3 cells was carried out in the presence of
450 Z-VAD-FMK (Selleckchem, Houston, USA) at 20 μM, or mock treatment with vehicle (DMSO),
451 added to cell cultures after virus adsorption. 10^6 collected cells were washed with PBS, and
452 fixation, permeabilization, and staining were carried out using BD Cytofix/Cytoperm™

453 Fixation/Permeabilization Kit (BD Biosciences), following the manufacturer's instructions.
454 Immunolabelling of intracellular active caspase-3 was performed with anti-cleaved caspase-3
455 (Asp175) (Clone 5A1E; #9664; Cell Signaling, 1:400) and secondary donkey anti-rabbit IgG
456 conjugated to Alexa Fluor 488 (AF488, Molecular Probes, 1:2500).
457
458 Flow cytometric acquisitions were performed in a FACSVerse (BD Biosciences, San Jose, CA,
459 USA) flow cytometer.
460
461 **$TCID_{50}$ quantification of viable viral particles.** 10^6 isolated CoV2-AC and their equivalent
462 purified conditioned supernatants, obtained as described above, were lysed by snap freeze-and-
463 thaw. To estimate viral load in apoptotic cells isolated by annexin V labeling, all infected cells
464 were collected, centrifuged at 300 *g* for 5 min, followed by magnetic separation with annexin V
465 MicroBeads (Miltenyi Biotec) according to the manufacturer's protocol. 10^6 pre-sorted cells,
466 annexin$^+$ cells, and annexin$^-$ cells were lysed by freeze-and-thaw for quantification. Viral loads
467 were estimated by titration in Vero CCL81 cells seeded onto 96-well plates and expressed as
468 50% tissue culture infectious dose ($TCID_{50}$). Quantification was performed with the Reed-
469 Muench method and plotted as $TCID_{50}$ units per mL(REED and MUENCH, 1938)
470
471 ***In vitro* assays with THP-1- and PBMC-derived macrophages.** 10^6 THP-1- and PBMC-
472 derived macrophages seeded on 24-well tissue culture plates were rinsed with warm PBS before
473 stimulation. Macrophage cultures were then topped with UV-AC, CoV2-AC, or Coxsackie-AC
474 resuspended in the appropriate serum-containing macrophage media at a 1:1 ratio. For
475 stimulation with conditioned supernatants, CoV2-AC-Sup were added directly to macrophages

476 cultures and topped with fresh media for volume adjustment. Infection with SARS-CoV-2 or
477 Coxsackie virus was carried out with virus adsorption at MOI 1 in serum-free media for 1 h
478 before topping with fresh serum-containing media. To block AC ligation and efferocytosis,
479 CoV2-AC were pre-incubated with 0.1 or 0.01 µg/mL of annexin-V (BD Biosciences) following
480 the manufacturer's recommendations prior to incubation with macrophages. To block AC
481 internalization, macrophages were pre-treated for 30 min, and incubation was carried out in the
482 presence of Cytochalasin D (10µM, Sigma). Macrophage cultures were rinsed out 2h after
483 incubation to remove unbound AC, topped with fresh media, and stimulation was carried on up
484 to supernatant collection to dose cytokines. At the time points described in the legend of the
485 figures, macrophages were rinsed at least twice with warm PBS to remove cell debris before
486 proceeding to analysis.
487
488 For gene expression analysis by RT-qPCR, rinsed macrophage cultures were lysed in appropriate
489 lysis buffer, as described below, and immediately frozen at -80°C.
490
491 To estimate CD206 surface expression, rinsed macrophages were removed with a cell scraper,
492 spun at 300 *g* for 5 min, washed with PBS, followed by incubation with rat serum (1:2000) for 5
493 min at room temperature (RT) and cell surface staining for 15 minutes at 4°C. Cells were labeled
494 with Zombie Violet™ Fixable Viability Kit (Biolegend) and anti-CD206-FITC antibody (clone
495 19.2, BD Biosciences). The cells were then fixed with 2% PFA for 10 min and washed before
496 flow cytometric analyses in a FACSVerse (BD Biosciences) flow cytometer.
497
498 For immunofluorescence imaging of efferocytosis, human monocyte-derived macrophages

499 seeded onto 13mm round coverslips were incubated with UV-AC or CoV2-AC labeled with 5
500 µM CellTrace™ CFSE dye (Thermo Scientific) for 2h. After rinsing out non-engulfed AC,
501 macrophages were fixed for 20 min with PBS 2% PFA at room temperature (RT). Cells were
502 then permeabilized with 0.1% Triton-X-100 in PBS for 10 min at room temperature (RT). Next,
503 cells were rinsed twice in PBS and incubated with PBS 1% bovine serum albumin (BSA) and 5
504 µg/mL normal donkey IgG (Jackson ImmunoResearch) for 45 min RT prior to overnight (ON)
505 incubation at 4ºC with primary antibodies: rabbit polyclonal anti-SARS-CoV-2 spike
506 glycoprotein antibody (ab272504 – Abcam, 1:1000) and Mouse mAb anti-Rat CD11b (clone
507 OX42; ab1211, Abcam, 1:300) diluted in PBS containing 1% BSA. Next, coverslips were
508 washed with PBS, and the following secondary antibodies were used for immunofluorescence:
509 Next, cells were rinsed thoroughly in PBS and incubated for 30 min at RT with the secondary
510 antibodies diluted in PBS: donkey anti-rabbit IgG F(ab)´$_2$-Alexa 594 (1:1000; Thermo Fisher
511 Scientific) and donkey anti-mouse IgG F(ab)´$_2$-Alexa 647 (1:1000; Thermo Fisher Scientific).
512 Cell nuclei were stained with Hoechst 33342. Cells were then rinsed, and coverslips mounted on
513 glass slides with Fluoromount-G (Invitrogen). Samples were analyzed using a Zeiss LSM 780
514 laser scanning confocal microscope (Carl Zeiss).
515
516 For the engulfment assays by flow cytometry, macrophages were labeled with 5 µM CellTrace™
517 Violet dye (CTV, Thermo Scientific), according to the manufacturer's recommendations.
518 CellTrace™ Violet (CTV)-labeled macrophages were stimulated with UV-AC or CoV2-AC
519 previously stained with 1 µM CellTrace™ Far Red dye (CTFR, Thermo Scientific), or 5 µM
520 CellTrace™ CFSE dye, as described in the legend of the figures. Following the removal of
521 unbound AC, macrophages were collected with a cell scraper, fixed with 2% PFA for 10 min,

522 and washed before proceeding with the acquisition by flow cytometry. For the two-round
523 efferocytosis assay, first-round UV-AC and CoV2-AC were labeled with a pH indicator
524 fluorogenic intracellular probe (pHrodo Red AM Intracellular pH Indicator - Thermo Scientific).
525 Second-round apoptotic Jurkat cells (UV-Jurkat) were generated by UV-C irradiation at 20
526 mJ/cm^2, followed by labeling with 1 μM CTFR and incubation at 37°C and 5% CO_2 for 6h.
527 CTV-labelled THP-1 cells were incubated with pHrodo-UV-AC or pHrodo-CoV2-AC for 18h at
528 a 1:1 ratio. Cells were then rinsed three times with PBS to remove non-engulfed AC, and CTV-
529 labelled Jurkat-AC were added to the culture at a 1:1 ratio for 2h. Macrophage cultures were
530 collected with a cell scraper, washed, fixed with 2% PFA for 10 min, and washed before
531 proceeding with the acquisition by flow cytometry. Flow cytometric acquisition was performed
532 in a FACSVerse (BD Biosciences) flow cytometer.
533
534 **Phenotyping of blood monocytes.** Blood samples from healthy donors and COVID-19 patients
535 were processed for erythrocyte lysis with ACK buffer, followed by incubation with Fc blocking
536 (BD Pharmingen) for 5 min at RT and labelling with monoclonal antibodies for CD14 (clone
537 M5E2; BD Pharmingen™), CD16 (clone ebioCB16(CB16); eBioscience Inc., San Diego; USA),
538 CD36 (clone CB38; BD Pharmingen™), HLA-DR (clone L243; BD Pharmingen™), CD3 (clone
539 SK7; BD Pharmingen™), CD19 (clone 6D5; BD Pharmingen™), CD56 (clone NCAM16.2; BD
540 Pharmingen™) and Fixable Viability Dye eFluor 780 (eBioscience) for 30 min at 4°C. The cells
541 were then washed with PBS and fixed with 2% PFA for 10 min before analyses in a FACSVerse
542 (BD Biosciences) flow cytometer.
543

544 ***In vitro* efferocytosis assay with monocytes from COVID-19 patients.** 10^6 PBMC from
545 healthy donors or COVID patients were plated onto eight-well chamber slides (Tek Chamber
546 Slide, Thermo Scientific) for monocyte adherence, followed by 24h incubation in RPMI
547 supplemented with 10% heat-inactivated human serum before stimulation. For induction of
548 apoptosis in thymocytes, cells isolated from C57BL/6 mice were resuspended in DMEMc and
549 treated with 20 mJ/cm^2 ultraviolet C irradiation and incubated for 6h at 37°C in a 5% CO_2.
550 Monocytes were incubated with apoptotic thymocytes at 1:5 ratio for 1h or zymosan A particles
551 (Thermo Scientific) at 1:1 ratio for 20 min at 37°C and 5% CO_2. The cells were then washed
552 with PBS at least three times to remove unbound apoptotic cells and zymosan particles, followed
553 by fixation with 4% PFA PBS solution for 15 min and rinsed twice with 0.01% Tween-20 Tris-
554 buffered saline (TBS). After permeabilization (0.1% Triton-X-100 in TBS for 3 min at RT), cells
555 were labeled with phalloidin conjugated to Alexa Fluor 488 (Thermo Scientific) and Hoechst
556 33342, and coverslips mounted with Fluoromount-G. Immunofluorescence and phase-contrast
557 images were acquired with 40x objective lens of Leica DMI4000B microscope (Leica
558 Microsystems; Heidelberg, Germany). To quantify AC engulfment, monocytes were identified
559 by nuclei morphology and membrane boundary, and AC uptake was enumerated using nuclei
560 fragmentation in the internalized thymocytes and transient F-actin reorganization around the
561 engulfed AC as criteria (Mylvaganam et al., 2021; Satyanarayanan et al., 2019). Quantification
562 was performed by the same researcher blinded to sample identification, and at least 10 fields and
563 minimum 30 cells were counted per sample. Phagocytic index, as a normalization by the average
564 percentage of uptake in control samples, was used to account for inherited differences between
565 experiments performed on different days. The representative images were obtained using a Zeiss
566 LSM 780 laser scanning confocal microscope (Carl Zeiss, Heidelberg, Germany).

567

568 **Cytokine quantification.** IL-6 and IL-1β cytokine levels in macrophage supernatants were
569 evaluated by ELISA assay (R&D Systems, Minneapolis, MN, EUA) or BD™ Cytometric Bead
570 Array (CBA) (#551811, BD Biosciences), as indicated in the legend of the figures, following the
571 manufacturers' recommendations. The cytokine levels in culture supernatants were evaluated by
572 CBA. IL-1β, IL-6, IL-8, IL-10, IL-12, and TNF-α detection in serum from healthy donors and
573 patients with COVID-19 were performed with CBA.

574

575 **RNA isolation and gene expression analyses.** Total RNA extraction of PBMC from healthy
576 donors or COVID-19 patients was performed using PureLink™ RNA Mini Kit (Ambion Inc.,
577 ThermoFisher Scientific), following the manufacturer's recommendations. Reverse transcription
578 was performed using the High Capacity cDNA Reverse Transcriptase Kit (Applied
579 Biosystems™, Foster City, USA), following the manufacturer's recommendations.

580

581 Total RNA extraction for human monocyte- or THP-1-derived macrophages stimulated *in vitro*
582 was performed using Directzol™ RNA miniPrep Kit (Zymo Research, Irvine, CA, USA),
583 following the manufacturer's recommendations. Reverse transcriptase was performed using M-
584 MLV reverse transcriptase (ThermoFisher Scientific) according to the manufacturer's
585 recommendations.

586

587 Gene expression RT-qPCR was performed using SybrGreen Master Mix (Applied Biosystems).
588 RT-qPCR was performed in fast mode, following the manufacturer's recommendations. The

589 evaluation of each gene expression was determined by the comparative CT method. Primer

590 sequences used were:

591

Gene	5' Forward	3' Reverse
CCL18	CTCTGCTGCCTCGTCTATACCT	CTTGGTTAGGAGGATGACACCT
CD163	GCGGGAGAGTGGAAGTGAAAG	GTTACAAATCACAGAGACCGCT
CD36	GGGAAAGTCACTGCGACATG	TGCAATACCTGGCTTTTCTCA
GAPDH	GTCTCCTCTGACTTCAACAGCG	ACCACCCTGTTGCTGTAGCCAA
IL6	GGTACATCCTCGACGGCATCT	GTGCCTCTTTGCTGCTTTCAC
ITGB5	AACCAGAGCGTGTACCAGAA	AGGAGAAGTTGTCGCACTCA
MERTK	CTCTGGCGTAGAGCTATCACT	AGGCTGGGTTGGTGAAAACA
MMP9	TGTACCGCTATGGTTACACTCG	GGCAGGGACAGTTGCTTCT
MRC1	AGCCAACACCAGCTCCTCAAGA	CAAAACGCTCGCGCATTGTCCA
PPARγ	ACCAAAGTGCAATCAAAGTGGA	ATGAGGGAGTTGGAAGGCTCT
SRA-1	GCAGTGGGATCACTTTCACAA	AGCTGTCATTGAGCGAGCATC
TIM4	ACAGGACAGATGGATGGAATA CCC	AGCCTTGTGTGTTTCTGCG

592

593 **Histological analysis**. Ultrasound-guided minimally invasive autopsies for COVID-19 deceased

594 patients were approved by the Research Ethics Committee of Hospital das Clínicas de Ribeirão

595 Preto (CEP, protocol no. 4.089.567). Non-neoplasic sections of lung parenchyma were obtained

596 from lobectomies for lung cancer as a control group (Rodrigues et al., 2020). Paraffin sections

597 from lungs were collected and processed as previously described (Rodrigues et al., 2020).

598 Sections were rinsed in PBS, and the antigen retrieval was performed by incubation of samples

599 with 0.1% trypsin (ThermoFisher Scientific) in PBS at 37ºC for 15 min. Next, sections were

600 rinsed and incubated with Image-iT FX Signal Enhancer (ThermoFisher Scientific) for 30 min at

601 RT. Sections were then rinsed in PBS and incubated for 45 min at RT in PBS containing 0.5%

602 BSA and 5µg/mL normal donkey IgG (Jackson ImmunoResearch).

603

604 For analysis of active caspase 3, lung sections were labeled with primary antibodies diluted in
605 PBS and incubated overnight ON at 4ºC: rabbit polyclonal anti-human cleaved caspase 3
606 (Asp175) (Clone 5A1E; #9664; Cell Signaling; 1:1000) and mouse anti-dsRNA (1:1000). Then,
607 sections were rinsed thoroughly in PBS and incubated for 45 min at RT with the secondary
608 antibodies: donkey anti-rabbit IgG conjugated to Alexa 594 (1:500; Thermo Fisher Scientific)
609 and donkey anti-mouse IgG F(ab)´$_2$-Alexa 488 (1:500; Thermo Fisher Scientific) diluted in PBS.
610 Sections were then rinsed, and coverslips mounted with DAPI Fluoromount-G (EM Sciences).
611 For *in situ* efferocytosis analysis, lung sections were labeled with primary antibodies diluted in
612 PBS and incubated overnight ON at 4ºC: mouse mAb anti-human CD68 (Clone KP1; Dako;
613 1:100), rabbit mAb anti-human cytokeratin 18 (Clone N1N3; GeneTex, 1:500) and anti-Spike
614 (rabbit polyclonal anti-SARS-CoV-2 Spike glycoprotein antibody, ab272504 – Abcam; 1:80)
615 previously conjugated to FITC (FITC Conjugation Kit-Lightning-Link®, Abcam, according to
616 the manufacturer's instructions). Then, sections were rinsed thoroughly in PBS and incubated for
617 45 min at RT with the secondary antibodies: donkey anti-rabbit IgG conjugated to Alexa 594
618 (1:500; Thermo Fisher Scientific) and donkey anti-mouse IgG F(ab)´$_2$-Alexa 647 (1:500; Thermo
619 Fisher Scientific) diluted in PBS. Next, sections were incubated for 15 min at RT with Hoechst
620 33342 (Invitrogen), rinsed in PBS, and mounted on glass slides with Fluoromount-G
621 (Invitrogen). Samples from active caspase 3 and *in situ* efferocytosis experiments were analyzed
622 using an ECLIPSE Ti2 Series microscope (Nikon).
623
624 For CD36 or MERTK expression analysis, lung sections were labeled with the primary
625 antibodies diluted in PBS and incubated overnight ON at 4ºC: rabbit polyclonal anti-human
626 CD36 (PA5-81996; 1:100 ThermoFisher Scientific) or rabbit mAb anti-human MERTK (Clone

627 SR29-07; 1:150; ThermoFisher Scientific) and mouse mAb anti-human calprotectin (Clone
628 MAC387; MA1-81381; 1:100; ThermoFisher Scientific). Then, sections were rinsed thoroughly
629 in PBS and incubated for 45 min at RT with the secondary antibodies donkey anti-rabbit IgG
630 conjugated to Alexa 488 (1:500; Thermo Fisher Scientific) and goat anti-mouse IgG conjugated
631 to Alexa 594 (Jackson ImmunoResearch) diluted in PBS. Sections were then rinsed, and
632 coverslips mounted with DAPI Fluoromount-G. Samples were analyzed using an Olympus BX61
633 Fluorescence Motorized Slide Scanner Microscope Pred VS120 (Olympus, Hamburg, Germany).
634
635 **Re-analysis of scRNA-seq Data**. We re-analyzed single-cell transcriptomic data from
636 bronchoalveolar lavage fluid (BAL) from patients with varying severity of COVID-19 disease
637 and their respective healthy controls (Liao et al., 2020). The dataset is publicly available at
638 https://covid19-balf.cells.ucsc.edu/. Downloaded data was imported into R environment version
639 v3.6.3. Differential expression analysis was conducted using FindMarkers function in Seurat
640 using the Wilcoxon test to compare mild and severe COVID-19 patients with healthy individuals
641 for each cluster previously identified by authors. Differentially expressed genes between
642 mild/severe COVID-19 patients and controls for each cluster were identified considering genes
643 expressed in at least 5% of cells and FDR < 0.05 and |avg_logFC| > 0.1. In addition, a
644 differentially expressed gene list comparing infected (identified SARS-Cov-2 transcripts) against
645 non-infected alveolar macrophages were obtained from supplemental materials from (Ren et al.,
646 2021). Gene Set Enrichment Analysis (GSEA) was performed using ClusterProfiler and fgsea R
647 packages (Korotkevich et al., 2021; Wu et al., 2021) for each differentially expressed gene or
648 log2 fold-change lists from Liao et al. (2020) and Ren et al. (2021) dataset. A custom gene set
649 was also utilized as a reference for GSEA, incorporating GO:0006911, GO:0043277 gene

650 ontology terms, and additional efferocytic related genes from the literature (Penberthy and
651 Ravichandran, 2016; Boada-Romero et al., 2020) (**Table S1**). Significantly enriched sets were
652 identified considering terms with p-value < 0.05.
653
654 **Data processing, quantification, and statistical analyses.** Flow cytometric data processing was
655 performed using FlowJo_V10 software (BD Biosciences). Images obtained by confocal and
656 epifluorescence microscopy were analyzed using ImageJ (NIH). Data were plotted and analyzed
657 with GraphPad Prism 8.4.2 software (GraphPad Prism Software Inc., San Diego, CA). The
658 statistical tests used are listed in the legend of the figures. For the *in vitro* assays, we used
659 Student's t-test to compare two experimental groups or one-way ANOVA, followed by ordinary
660 ANOVA and multiple comparison correction, to compare three or more experimental groups.
661 For the comparison between COVID-19 patients and healthy control datasets, normality tests
662 were performed, and samples with non-Gaussian distribution were analyzed applying the Mann–
663 Whitney test. For monocyte phenotyping from blood samples, the outliers were identified
664 applying the ROUT method defining Q = 0.1% and then removed from the analyses. p values <
665 0.05 were considered significant.
666
667 **Acknowledgements**
668 The authors thank Denise M. da Fonseca, Elizabete R. Milani and Roberta R. C. Rosales
669 (FMRP-USP) for technical assistance and Jennifer Martinez (NIEHS, NIH) for thoughtful
670 insights and discussions.
671
672 **Funding**: This work was supported by grants from:

Fundação de Amparo a Pesquisa do Estado de São Paulo (FAPESP) grants 2018/25559-4 and 2020/05288-6 (L.D.C)

Coordenação de Aperfeiçoamento de Pessoal de Nível Superior (CAPES) grant 88887.507253/2020-00 (D. S. Z. and L.D.C.)

Conselho Nacional de Desenvolvimento Científico e Tecnológico (CNPq) grant 434538/2018-3 (L.D.C.)

D.S., A. C. G. S., T. S. R. are supported by FAPESP fellowships.

Author Contributions

Conceptualization: A. C. G. S., D. S., T. S. R., and L.D.C.

Methodology: A. C. G. S., D. S., T. S. R. and L.D.C

Investigation and data analysis: A. C. G. S., D. S., T. S. R.

Investigation and data analysis – specific experiments: M. F. R., E. G. F. F., D. L. A. T., M. H. F. L., D. B. C. N., and I. M. S. C.

Clinical data curation: N. B. A., M. C. G., L. P. B., M I. F. L., M. N. B., S. S. B., R. C. S., F. C. V., M. A. M., R. L. A., S. C. L. A, F. R. O., A. T. F., P. L. J. and R. D. R. O

Clinical data analysis: P. L. J. and R. D. R. O

Resources: C. M. S., J. E. T., A. B., S. O., D. B. C., L. A., A. Y. I , T. M. L., R. B. M., F. V., E. A., T. M. C., J. C. A. F., A.T.F., H. I. N., D. S. Z., P. L. J. and R. D. R. O

Visualization: A.C.G.S., D. S. and I. C.

Funding acquisition and supervision: L. D. C.

Writing – original draft: D. S., A. C. G. S., T. S. R., and L. D. C

Writing – review and editing: all authors

Competing Interests

The authors declare no competing financial interests.

Data Availability

All data are available in the main text or supporting information.

References

A-Gonzalez N, Quintana JA, García-Silva S, Mazariegos M, Aleja AG de la, Nicolás-Ávila JAA, Walter W, Adrover JM, Crainiciuc G, Kuchroo VK, Rothlin CV, Peinado H, Castrillo A, Ricote M, Hidalgo A. 2017. Phagocytosis imprints heterogeneity in tissue-resident macrophages. *The Journal of experimental medicine* 214:1281–1296. doi:10.1084/jem.20161375

Banerjee S, Friggeri A, Liu G, Abraham E. 2010. The C-terminal acidic tail is responsible for the inhibitory effects of HMGB1 on efferocytosis. *J Leukocyte Biol* 88:973–979. doi:10.1189/jlb.0510262

Bastard P, Rosen LB, Zhang Q, Michailidis E, Hoffmann H-H, Zhang Y, Dorgham K, Philippot Q, Rosain J, Béziat V, Manry J, Shaw E, Haljasmägi L, Peterson P, Lorenzo L, Bizien L, Trouillet-Assant S, Dobbs K, Jesus AA de, Belot A, Kallaste A, Catherinot E, Tandjaoui-Lambiotte Y, Pen JL, Kerner G, Bigio B, Seeleuthner Y, Yang R, Bolze A, Spaan AN, Delmonte OM, Abers MS, Aiuti A, Casari G, Lampasona V, Piemonti L, Ciceri F, Bilguvar K, Lifton RP, Vasse M, Smadja DM, Migaud M, Hadjadj J, Terrier B, Duffy D, Quintana-Murci L, Beek D van de, Roussel L, Vinh DC, Tangye SG, Haerynck F, Dalmau D, Martinez-Picado J, Brodin P, Nussenzweig MC, Boisson-Dupuis S, Rodríguez-Gallego C, Vogt G, Mogensen TH, Oler AJ, Gu J, Burbelo PD, Cohen J, Biondi A, Bettini LR, D'Angio M, Bonfanti P, Rossignol P, Mayaux J, Rieux-Laucat F, Husebye ES, Fusco F, Ursini MV, Imberti L, Sottini A, Paghera S, Quiros-Roldan E, Rossi C, Castagnoli R, Montagna D, Licari A, Marseglia GL, Duval X, Ghosn J, Lab§ H, Group§ N-UIR to C, Clinicians§ C, Clinicians§ C-S, Group§ IC, Group§ FCCS, Consortium§ TMI, Cohort§ C-C, Biobank§ AUC-19, Effort§ CHG, Tsang JS, Goldbach-Mansky R, Kisand K, Lionakis MS, Puel A, Zhang S-Y, Holland SM, Gorochov G, Jouanguy E, Rice CM, Cobat A, Notarangelo LD, Abel L, Su HC, Casanova J-L. 2020. Auto-antibodies against type I IFNs in patients with life-threatening COVID-19. *Science* eabd4585. doi:10.1126/science.abd4585

Blanco-Melo D, Nilsson-Payant BE, Liu W-C, Uhl S, Hoagland D, Møller R, Jordan TX, Oishi K, Panis M, Sachs D, Wang TT, Schwartz RE, Lim JK, Albrecht RA, tenOever BR. 2020.

733 Imbalanced Host Response to SARS-CoV-2 Drives Development of COVID-19. *Cell*
734 181:1036-1045.e9. doi:10.1016/j.cell.2020.04.026
735 Boada-Romero E, Martinez J, Heckmann B, Green D. 2020. The clearance of dead cells by
736 efferocytosis. *Nat Rev Mol Cell Bio* 1–17. doi:10.1038/s41580-020-0232-1
737 Bosurgi L, Cao YG, Cabeza-Cabrerizo M, Tucci A, Hughes LD, Kong Y, Weinstein JS, Licona-
738 Limon P, Schmid ET, Pelorosso F, Gagliani N, Craft JE, Flavell RA, Ghosh S, Rothlin CV.
739 2017. Macrophage function in tissue repair and remodeling requires IL-4 or IL-13 with
740 apoptotic cells. *Sci New York N Y* 356:1072–1076. doi:10.1126/science.aai8132
741 Chan JF-W, Zhang AJ, Yuan S, Poon VK-M, Chan CC-S, Lee AC-Y, Chan W-M, Fan Z, Tsoi
742 H-W, Wen L, Liang R, Cao J, Chen Y, Tang K, Luo C, Cai J-P, Kok K-H, Chu H, Chan K-H,
743 Sridhar S, Chen Z, Chen H, To KK-W, Yuen K-Y. 2020. Simulation of the Clinical and
744 Pathological Manifestations of Coronavirus Disease 2019 (COVID-19) in a Golden Syrian
745 Hamster Model: Implications for Disease Pathogenesis and Transmissibility. *Clin Infect Dis*
746 *Official Publ Infect Dis Soc Am* 71:2428–2446. doi:10.1093/cid/ciaa325
747 Chen L, Long X, Xu Q, Tan J, Wang G, Cao Y, Wei J, Luo H, Zhu H, Huang Liang, Meng F,
748 Huang Lifang, Wang N, Zhou X, Zhao L, Chen X, Mao Z, Chen C, Li Z, Sun Z, Zhao J,
749 Wang D, Huang G, Wang W, Zhou J. 2020. Elevated serum levels of S100A8/A9 and
750 HMGB1 at hospital admission are correlated with inferior clinical outcomes in COVID-19
751 patients. *Cell Mol Immunol* 17:992–994. doi:10.1038/s41423-020-0492-x
752 Chu H, Chan JF-W, Yuen TT-T, Shuai H, Yuan S, Wang Y, Hu B, Yip CC-Y, Tsang JO-L,
753 Huang X, Chai Y, Yang D, Hou Y, Chik KK-H, Zhang X, Fung AY-F, Tsoi H-W, Cai J-P,
754 Chan W-M, Ip JD, Chu AW-H, Zhou J, Lung DC, Kok K-H, To KK-W, Tsang OT-Y, Chan
755 K-H, Yuen K-Y. 2020. Comparative tropism, replication kinetics, and cell damage profiling
756 of SARS-CoV-2 and SARS-CoV with implications for clinical manifestations,
757 transmissibility, and laboratory studies of COVID-19: an observational study. *Lancet Microbe*
758 1:e14–e23. doi:10.1016/s2666-5247(20)30004-5
759 Chu H, Shuai H, Hou Y, Zhang X, Wen L, Huang X, Hu B, Yang D, Wang Y, Yoon C, Wong
760 BH-Y, Li C, Zhao X, Poon VK-M, Cai J-P, Wong KK-Y, Yeung M-L, Zhou J, Au-Yeung
761 RK-H, Yuan S, Jin D-Y, Kok K-H, Perlman S, Chan JF-W, Yuen K-Y. 2021. Targeting
762 highly pathogenic coronavirus-induced apoptosis reduces viral pathogenesis and disease
763 severity. *Sci Adv* 7:eabf8577. doi:10.1126/sciadv.abf8577
764 Cohen PL, Caricchio R, Abraham V, Camenisch TD, Jennette JC, Roubey RAS, Earp HS,
765 Matsushima G, Reap EA. 2002. Delayed Apoptotic Cell Clearance and Lupus-like
766 Autoimmunity in Mice Lacking the c-mer Membrane Tyrosine Kinase. *J Exp Medicine*
767 196:135–140. doi:10.1084/jem.20012094
768 Corman VM, Landt O, Kaiser M, Molenkamp R, Meijer A, Chu DK, Bleicker T, Brünink S,
769 Schneider J, Schmidt ML, Mulders DG, Haagmans BL, Veer B van der, Brink S van den,
770 Wijsman L, Goderski G, Romette J-L, Ellis J, Zambon M, Peiris M, Goossens H, Reusken C,
771 Koopmans MP, Drosten C. 2020. Detection of 2019 novel coronavirus (2019-nCoV) by real-
772 time RT-PCR. *Eurosurveillance* 25:2000045. doi:10.2807/1560-7917.es.2020.25.3.2000045
773 Doran AC, Yurdagul A, Tabas I. 2020. Efferocytosis in health and disease. *Nat Rev Immunol*
774 20:254–267. doi:10.1038/s41577-019-0240-6
775 Fadok VA, Voelker DR, Campbell PA, Cohen JJ, Bratton DL, Henson PM. 1992. Exposure of
776 phosphatidylserine on the surface of apoptotic lymphocytes triggers specific recognition and
777 removal by macrophages. *J Immunol Baltim Md 1950* 148:2207–16.

778 Feng X, Deng T, Zhang Y, Su S, Wei C, Han D. 2011. Lipopolysaccharide inhibits macrophage
779 phagocytosis of apoptotic neutrophils by regulating the production of tumour necrosis factor α
780 and growth arrest-specific gene 6. *Immunology* 132:287–295. doi:10.1111/j.1365-
781 2567.2010.03364.x
782 Gomes R, Guerra-Sá R, Arruda E. 2009. Coxsackievirus B5 induced apoptosis of HeLa cells:
783 effects on p53 and SUMO. *Virology* 396:256–63. doi:10.1016/j.virol.2009.10.005
784 Hamers AAJ, Dinh HQ, Thomas GD, Marcovecchio P, Blatchley A, Nakao CS, Kim C,
785 McSkimming C, Taylor AM, Nguyen AT, McNamara CA, Hedrick CC. 2019. Human
786 Monocyte Heterogeneity as Revealed by High-Dimensional Mass Cytometry. *Arteriosclerosis*
787 *Thrombosis Vasc Biology* 39:25–36. doi:10.1161/atvbaha.118.311022
788 Han Y, Zhang H, Mu S, Wei W, Jin C, Xue Y, Tong C, Zha Y, Song Z, Gu G. 2020. Lactate
789 dehydrogenase, a Risk Factor of Severe COVID-19 Patients. *Medrxiv* 2020.03.24.20040162.
790 doi:10.1101/2020.03.24.20040162
791 Jamieson AM, Pasman L, Yu S, Gamradt P, Homer RJ, Decker T, Medzhitov R. 2013. Role of
792 Tissue Protection in Lethal Respiratory Viral-Bacterial Coinfection. *Science* 340:1230–1234.
793 doi:10.1126/science.1233632
794 Korotkevich G, Sukhov V, Budin N, Shpak B, Artyomov MN, Sergushichev A. 2021. Fast gene
795 set enrichment analysis. *Biorxiv* 060012. doi:10.1101/060012
796 Li Shaohua, Jiang L, Li X, Lin F, Wang Y, Li B, Jiang T, An W, Liu S, Liu H, Xu P, Zhao L,
797 Zhang L, Mu J, Wang H, Kang J, Li Y, Huang L, Zhu C, Zhao S, Lu J, Ji J, Zhao J. 2020.
798 Clinical and pathological investigation of patients with severe COVID-19. *Jci Insight* 5.
799 doi:10.1172/jci.insight.138070
800 Li Shufen, Zhang Y, Guan Z, Li H, Ye M, Chen X, Shen J, Zhou Y, Shi Z-L, Zhou P, Peng K.
801 2020. SARS-CoV-2 triggers inflammatory responses and cell death through caspase-8
802 activation. *Signal Transduct Target Ther* 5:235. doi:10.1038/s41392-020-00334-0
803 Liao M, Liu Y, Yuan J, Wen Y, Xu G, Zhao J, Cheng L, Li J, Wang X, Wang F, Liu L, Amit I,
804 Zhang S, Zhang Z. 2020. Single-cell landscape of bronchoalveolar immune cells in patients
805 with COVID-19. *Nat Med* 26:842–844. doi:10.1038/s41591-020-0901-9
806 Lucas C, Wong P, Klein J, Castro TBR, Silva J, Sundaram M, Ellingson MK, Mao T, Oh JE,
807 Israelow B, Takahashi T, Tokuyama M, Lu P, Venkataraman A, Park A, Mohanty S, Wang
808 H, Wyllie AL, Vogels CBF, Earnest R, Lapidus S, Ott IM, Moore AJ, Muenker MC, Fournier
809 JB, Campbell M, Odio CD, Casanovas-Massana A, Obaid A, Lu-Culligan A, Nelson A, Brito
810 A, Nunez A, Martin A, Watkins A, Geng B, Kalinich C, Harden C, Todeasa C, Jensen C, Kim
811 D, McDonald D, Shepard D, Courchaine E, White EB, Song E, Silva E, Kudo E, DeIuliis G,
812 Rahming H, Park H-J, Matos I, Nouws J, Valdez J, Fauver J, Lim J, Rose K-A, Anastasio K,
813 Brower K, Glick L, Sharma L, Sewanan L, Knaggs L, Minasyan M, Batsu M, Petrone M,
814 Kuang M, Nakahata M, Campbell M, Linehan M, Askenase MH, Simonov M, Smolgovsky
815 M, Sonnert N, Naushad N, Vijayakumar P, Martinello R, Datta R, Handoko R, Bermejo S,
816 Prophet S, Bickerton S, Velazquez S, Alpert T, Rice T, Khoury-Hanold W, Peng X, Yang Y,
817 Cao Y, Strong Y, Herbst R, Shaw AC, Medzhitov R, Schulz WL, Grubaugh ND, Cruz CD,
818 Farhadian S, Ko AI, Omer SB, Iwasaki A. 2020. Longitudinal analyses reveal immunological
819 misfiring in severe COVID-19. *Nature* 584:463–469. doi:10.1038/s41586-020-2588-y
820 Martins R, Carlos AR, Braza F, Thompson JA, Bastos-Amador P, Ramos S, Soares MP. 2019.
821 Disease Tolerance as an Inherent Component of Immunity. *Annu Rev Immunol* 37:405–437.
822 doi:10.1146/annurev-immunol-042718-041739

823 Michlewska S, Dransfield I, Megson IL, Rossi AG. 2008. Macrophage phagocytosis of apoptotic
824 neutrophils is critically regulated by the opposing actions of pro-inflammatory and anti-
825 inflammatory agents: key role for TNF-alpha. *Faseb J Official Publ Fed Am Soc Exp Biology*
826 23:844–54. doi:10.1096/fj.08-121228
827 Miyanishi M, Tada K, Koike M, Uchiyama Y, Kitamura T, Nagata S. 2007. Identification of
828 Tim4 as a phosphatidylserine receptor. *Nature* 450:435–439. doi:10.1038/nature06307
829 Morioka S, Perry JSA, Raymond MH, Medina CB, Zhu Y, Zhao L, Serbulea V, Onengut-
830 Gumuscu S, Leitinger N, Kucenas S, Rathmell JC, Makowski L, Ravichandran KS. 2018.
831 Efferocytosis induces a novel SLC program to promote glucose uptake and lactate release.
832 *Nature* 563:714–718. doi:10.1038/s41586-018-0735-5
833 Mulay A, Konda B, Garcia G, Yao C, Beil S, Villalba JM, Koziol C, Sen C, Purkayastha A,
834 Kolls JayK, Pociask DA, Pessina P, Aja JS de, Garcia-de-Alba C, Kim CF, Gomperts B,
835 Arumugaswami V, Stripp BR. 2021. SARS-CoV-2 infection of primary human lung
836 epithelium for COVID-19 modeling and drug discovery. *Cell Reports* 35:109055.
837 doi:10.1016/j.celrep.2021.109055
838 Murray PJ, Wynn TA. 2011. Protective and pathogenic functions of macrophage subsets. *Nat*
839 *Rev Immunol* 11:723–737. doi:10.1038/nri3073
840 Mylvaganam S, Freeman SA, Grinstein S. 2021. The cytoskeleton in phagocytosis and
841 macropinocytosis. *Curr Biol* 31:R619–R632. doi:10.1016/j.cub.2021.01.036
842 Nagata S. 2018. Apoptosis and Clearance of Apoptotic Cells. *Annu Rev Immunol* 36:489–517.
843 doi:10.1146/annurev-immunol-042617-053010
844 Olagnier D, Lavergne R-A, Meunier E, Lefèvre L, Dardenne C, Aubouy A, Benoit-Vical F,
845 Ryffel B, Coste A, Berry A, Pipy B. 2011. Nrf2, a PPARγ Alternative Pathway to Promote
846 CD36 Expression on Inflammatory Macrophages: Implication for Malaria. *Plos Pathog*
847 7:e1002254. doi:10.1371/journal.ppat.1002254
848 Park D, Han CZ, Elliott MR, Kinchen JM, Trampont PC, Das S, Collins S, Lysiak JJ, Hoehn KL,
849 Ravichandran KS. 2011. Continued clearance of apoptotic cells critically depends on the
850 phagocyte Ucp2 protein. *Nature* 477:220–4. doi:10.1038/nature10340
851 Parks BW, Black LL, Zimmerman KA, Metz AE, Steele C, Murphy-Ullrich JE, Kabarowski JH.
852 2013. CD36, but not G2A, modulates efferocytosis, inflammation, and fibrosis following
853 bleomycin-induced lung injury[S]. *J Lipid Res* 54:1114–1123. doi:10.1194/jlr.m035352
854 Penberthy KK, Ravichandran KS. 2016. Apoptotic cell recognition receptors and scavenger
855 receptors. *Immunological reviews* 269:44–59. doi:10.1111/imr.12376
856 Peng Y, Elkon KB. 2011. Autoimmunity in MFG-E8–deficient mice is associated with altered
857 trafficking and enhanced cross-presentation of apoptotic cell antigens. *J Clin Invest*
858 121:2221–2241. doi:10.1172/jci43254
859 Perry JSA, Morioka S, Medina CB, Etchegaray JI, Barron B, Raymond MH, Lucas CD,
860 Onengut-Gumuscu S, Delpire E, Ravichandran KS. 2019. Interpreting an apoptotic corpse as
861 anti-inflammatory involves a chloride sensing pathway. *Nat Cell Biol* 21:1532–1543.
862 doi:10.1038/s41556-019-0431-1
863 Reed LJ, Muench H. 1938. A simple method of estimating fifty per cent endpoints. *Am J*
864 *Epidemiol* 27:493–497. doi:10.1093/oxfordjournals.aje.a118408
865 Ren X, Wen W, Fan X, Hou W, Su Bin, Cai P, Li J, Liu Y, Tang F, Zhang F, Yang Y, He
866 Jiangping, Ma W, He Jingjing, Wang P, Cao Q, Chen F, Chen Y, Cheng X, Deng G, Deng X,
867 Ding W, Feng Y, Gan R, Guo C, Guo W, He S, Jiang C, Liang J, Li Y, Lin J, Ling Y, Liu H,
868 Liu J, Liu N, Liu S-Q, Luo M, Ma Q, Song Q, Sun W, Wang G, Wang F, Wang Y, Wen X,

869 Wu Q, Xu G, Xie X, Xiong X, Xing X, Xu H, Yin C, Yu D, Yu K, Yuan J, Zhang B, Zhang
870 P, Zhang T, Zhao J, Zhao Peidong, Zhou J, Zhou W, Zhong S, Zhong X, Zhang S, Zhu L, Zhu
871 P, Zou B, Zou J, Zuo Z, Bai F, Huang X, Zhou P, Jiang Q, Huang Z, Bei J-X, Wei L, Bian X-
872 W, Liu X, Cheng T, Li X, Zhao Pingsen, Wang F-S, Wang H, Su Bing, Zhang Zheng, Qu K,
873 Wang X, Chen J, Jin R, Zhang Zemin. 2021. COVID-19 immune features revealed by a large-
874 scale single-cell transcriptome atlas. *Cell* 184:1895-1913.e19. doi:10.1016/j.cell.2021.01.053
875 Ren Y, Shu T, Wu D, Mu J, Wang C, Huang M, Han Y, Zhang X-Y, Zhou W, Qiu Y, Zhou X.
876 2020. The ORF3a protein of SARS-CoV-2 induces apoptosis in cells. *Cell Mol Immunol*
877 17:881–883. doi:10.1038/s41423-020-0485-9
878 Rodrigues TS, Sá KSG de, Ishimoto AY, Becerra A, Oliveira S, Almeida L, Gonçalves AV,
879 Perucello DB, Andrade WA, Castro R, Veras FP, Toller-Kawahisa JE, Nascimento DC, Lima
880 MHF de, Silva CMS, Caetite DB, Martins RB, Castro IA, Pontelli MC, Barros FC de, Amaral
881 NB do, Giannini MC, Bonjorno LP, Lopes MIF, Santana RC, Vilar FC, Auxiliadora-Martins
882 M, Luppino-Assad R, Almeida SCL de, Oliveira FR de, Batah SS, Siyuan L, Benatti MN,
883 Cunha TM, Alves-Filho JC, Cunha FQ, Cunha LD, Frantz FG, Kohlsdorf T, Fabro AT,
884 Arruda E, Oliveira RDR de, Louzada-Junior P, Zamboni DS. 2020. Inflammasomes are
885 activated in response to SARS-CoV-2 infection and are associated with COVID-19 severity
886 in patients. *J Exp Med* 218. doi:10.1084/jem.20201707
887 Rodriguez-Manzanet R, Sanjuan MA, Wu HY, Quintana FJ, Xiao S, Anderson AC, Weiner HL,
888 Green DR, Kuchroo VK. 2010. T and B cell hyperactivity and autoimmunity associated with
889 niche-specific defects in apoptotic body clearance in TIM-4-deficient mice. *Proc National*
890 *Acad Sci* 107:8706–8711. doi:10.1073/pnas.0910359107
891 Rothlin CV, Hille TD, Ghosh S. 2020. Determining the effector response to cell death. *Nat Rev*
892 *Immunol* 1–13. doi:10.1038/s41577-020-00456-0
893 Satyanarayanan SK, Kebir DE, Soboh S, Butenko S, Sekheri M, Saadi J, Peled N, Assi S,
894 Othman A, Schif-Zuck S, Feuermann Y, Barkan D, Sher N, Filep JG, Ariel A. 2019. IFN-β is
895 a macrophage-derived effector cytokine facilitating the resolution of bacterial inflammation.
896 *Nat Commun* 10:3471. doi:10.1038/s41467-019-10903-9
897 Schulte-Schrepping J, Reusch N, Paclik D, Baßler K, Schlickeiser S, Zhang B, Krämer B,
898 Krammer T, Brumhard S, Bonaguro L, Domenico ED, Wendisch D, Grasshoff M, Kapellos
899 TS, Beckstette M, Pecht T, Saglam A, Dietrich O, Mei HE, Schulz AR, Conrad C, Kunkel D,
900 Vafadarnejad E, Xu C-J, Horne A, Herbert M, Drews A, Thibeault C, Pfeiffer M, Hippenstiel
901 S, Hocke A, Müller-Redetzky H, Heim K-M, Machleidt F, Uhrig A, Jarcy LB de, Jürgens L,
902 Stegemann M, Glösenkamp CR, Volk H-D, Goffinet C, Landthaler M, Wyler E, Georg P,
903 Schneider M, Dang-Heine C, Neuwinger N, Kappert K, Tauber R, Corman V, Raabe J, Kaiser
904 KM, Vinh MT, Rieke G, Meisel C, Ulas T, Becker M, Geffers R, Witzenrath M, Drosten C,
905 Suttorp N, Kalle C von, Kurth F, Händler K, Schultze JL, Aschenbrenner AC, Li Y,
906 Nattermann J, Sawitzki B, Saliba A-E, Sander LE, (DeCOI) DC-19 OI, Angelov A, Bals R,
907 Bartholomäus A, Becker A, Bezdan D, Bonifacio E, Bork P, Clavel T, Colome-Tatche M,
908 Diefenbach A, Dilthey A, Fischer N, Förstner K, Frick J-S, Gagneur J, Goesmann A, Hain T,
909 Hummel M, Janssen S, Kalinowski J, Kallies R, Kehr B, Keller A, Kim-Hellmuth S, Klein C,
910 Kohlbacher O, Korbel JO, Kurth I, Landthaler M, Li Y, Ludwig K, Makarewicz O, Marz M,
911 McHardy A, Mertes C, Nöthen M, Nürnberg P, Ohler U, Ossowski S, Overmann J, Peter S,
912 Pfeffer K, Poetsch AR, Pühler A, Rajewsky N, Ralser M, Rieß O, Ripke S, Rocha UN da,
913 Rosenstiel P, Saliba A-E, Sander LE, Sawitzki B, Schiffer P, Schulte E-C, Schultze JL,
914 Sczyrba A, Stegle O, Stoye J, Theis F, Vehreschild J, Vogel J, Kleist M von, Walker A,

Walter J, Wieczorek D, Ziebuhr J. 2020. Severe COVID-19 Is Marked by a Dysregulated Myeloid Cell Compartment. *Cell* 182:1419-1440.e23. doi:10.1016/j.cell.2020.08.001

Siddiqi HK, Mehra MR. 2020. COVID-19 Illness in Native and Immunosuppressed States: A Clinical-Therapeutic Staging Proposal. *J Hear Lung Transplant*. doi:10.1016/j.healun.2020.03.012

Silvin A, Chapuis N, Dunsmore G, Goubet A-G, Dubuisson A, Derosa L, Almire C, Hénon C, Kosmider O, Droin N, Rameau P, Catelain C, Alfaro A, Dussiau C, Friedrich C, Sourdeau E, Marin N, Szwebel T-A, Cantin D, Mouthon L, Borderie D, Deloger M, Bredel D, Mouraud S, Drubay D, Andrieu M, Lhonneur A-S, Saada V, Stoclin A, Willekens C, Pommeret F, Griscelli F, Ng LG, Zhang Z, Bost P, Amit I, Barlesi F, Marabelle A, Pène F, Gachot B, André F, Zitvogel L, Ginhoux F, Fontenay M, Solary E. 2020. Elevated Calprotectin and Abnormal Myeloid Cell Subsets Discriminate Severe from Mild COVID-19. *Cell* 182:1401-1418.e18. doi:10.1016/j.cell.2020.08.002

Tait JF, Smith C. 1999. Phosphatidylserine Receptors: Role of CD36 in Binding of Anionic Phospholipid Vesicles to Monocytic Cells*. *J Biol Chem* 274:3048–3054. doi:10.1074/jbc.274.5.3048

Thorp E, Vaisar T, Subramanian M, Mautner L, Blobel C, Tabas I. 2011. Shedding of the Mer Tyrosine Kinase Receptor Is Mediated by ADAM17 Protein through a Pathway Involving Reactive Oxygen Species, Protein Kinase Cδ, and p38 Mitogen-activated Protein Kinase (MAPK). *J Biol Chem* 286:33335–33344. doi:10.1074/jbc.m111.263020

Valle DMD, Kim-Schulze S, Huang H-H, Beckmann ND, Nirenberg S, Wang B, Lavin Y, Swartz TH, Madduri D, Stock A, Marron TU, Xie H, Patel M, Tuballes K, Oekelen OV, Rahman A, Kovatch P, Aberg JA, Schadt E, Jagannath S, Mazumdar M, Charney AW, Firpo-Betancourt A, Mendu DR, Jhang J, Reich D, Sigel K, Cordon-Cardo C, Feldmann M, Parekh S, Merad M, Gnjatic S. 2020. An inflammatory cytokine signature predicts COVID-19 severity and survival. *Nat Med* 26:1636–1643. doi:10.1038/s41591-020-1051-9

Veras FP, Pontelli MC, Silva CM, Toller-Kawahisa JE, Lima M de, Nascimento DC, Schneider AH, Caetité D, Tavares LA, Paiva IM, Rosales R, Colón D, Martins R, Castro IA, Almeida GM, Lopes MIF, Benatti MN, Bonjorno LP, Giannini MC, Luppino-Assad R, Almeida SL, Vilar F, Santana R, Bollela VR, Auxiliadora-Martins M, Borges M, Miranda CH, Pazin-Filho A, Silva LLP da, Cunha L, Zamboni DS, Dal-Pizzol F, Leiria LO, Siyuan L, Batah S, Fabro A, Mauad T, Dolhnikoff M, Duarte-Neto A, Saldiva P, Cunha TM, Alves-Filho JC, Arruda E, Louzada-Junior P, Oliveira RD, Cunha FQ. 2020. SARS-CoV-2–triggered neutrophil extracellular traps mediate COVID-19 pathology. *J Exp Med* 217. doi:10.1084/jem.20201129

Wang Y, Subramanian M, Yurdagul A, Barbosa-Lorenzi VC, Cai B, Juan-Sanz J de, Ryan TA, Nomura M, Maxfield FR, Tabas I. 2017. Mitochondrial Fission Promotes the Continued Clearance of Apoptotic Cells by Macrophages. *Cell* 171:331-345.e22. doi:10.1016/j.cell.2017.08.041

Webb BJ, Peltan ID, Jensen P, Hoda D, Hunter B, Silver A, Starr N, Buckel W, Grisel N, Hummel E, Snow G, Morris D, Stenehjem E, Srivastava R, Brown SM. 2020. Clinical criteria for COVID-19-associated hyperinflammatory syndrome: a cohort study. *Lancet Rheumatology*. doi:10.1016/s2665-9913(20)30343-x

Wu T, Hu E, Xu S, Chen M, Guo P, Dai Z, Feng T, Zhou L, Tang W, Zhan L, Fu X, Liu S, Bo X, Yu G. 2021. clusterProfiler 4.0: A universal enrichment tool for interpreting omics data. *Innovation* 2:100141. doi:10.1016/j.xinn.2021.100141

960 Yurdagul A, Subramanian M, Wang X, Crown SB, Ilkayeva OR, Darville L, Kolluru GK,
961 Rymond CC, Gerlach BD, Zheng Z, Kuriakose G, Kevil CG, Koomen JM, Cleveland JL,
962 Muoio DM, Tabas I. 2020. Macrophage Metabolism of Apoptotic Cell-Derived Arginine
963 Promotes Continual Efferocytosis and Resolution of Injury. *Cell Metab* 31:518-533.e10.
964 doi:10.1016/j.cmet.2020.01.001
965 Zhu N, Wang Wenling, Liu Z, Liang C, Wang Wen, Ye F, Huang B, Zhao L, Wang H, Zhou W,
966 Deng Y, Mao L, Su C, Qiang G, Jiang T, Zhao J, Wu G, Song J, Tan W. 2020.
967 Morphogenesis and cytopathic effect of SARS-CoV-2 infection in human airway epithelial
968 cells. *Nat Commun* 11:3910. doi:10.1038/s41467-020-17796-z
969 Zuniga M, Gomes C, Carsons SE, Bender MT, Cotzia P, Miao QR, Lee DC, Rodriguez A. 2021.
970 Autoimmunity to Annexin A2 predicts mortality among hospitalised COVID-19 patients. *Eur*
971 *Respir J* 2100918. doi:10.1183/13993003.00918-2021
972 Zuo Y, Estes SK, Ali RA, Gandhi AA, Yalavarthi S, Shi H, Sule G, Gockman K, Madison JA,
973 Zuo M, Yadav V, Wang J, Woodard W, Lezak SP, Lugogo NL, Smith SA, Morrissey JH,
974 Kanthi Y, Knight JS. 2020. Prothrombotic autoantibodies in serum from patients hospitalized
975 with COVID-19. *Sci Transl Med* 12:eabd3876. doi:10.1126/scitranslmed.abd3876
976

977 **Figure captions**

978

979 **Figure 1. Macrophages engulf apoptotic cells carrying viable SARS-CoV-2**

980 **(A-B)** Representative histological findings in post-mortem lung tissue from COVID-19 patients,
981 obtained by ultrasound-guided minimally invasive autopsy. **(A)** Representative differential
982 interference contrast (upper panel) and immunofluorescence (middle panel) images of tissue from
983 P1 patient, immunolabelled with anti-cleaved caspase 3 (red), anti-dsRNA (SARS-CoV2, green),
984 and stained with DAPI (nuclei, blue) for the detection of caspase-3 activation in infected cells. The
985 bottom panels show higher magnification of the two selected areas. Arrows indicate cells positive
986 for both Cl-caspase-3 and dsRNA (purple arrows: ciliated pseudostratified epithelia of a
987 respiratory bronchiole; white arrows: type II pneumocytes; white arrowheads: type I pneumocytes;
988 *cleaved-Casp3^{+} non-epithelial cell). Tissues were scanned by wide-field epifluorescence
989 imaging. Scale bar: 50 µm. **(B)** Representative immunofluorescence image of tissue from P1
990 patient immunolabelled for the detection of efferocytosis in situ with anti-CD68 (detecting

991 macrophages, white), anti-cytokeratin18 (detecting epithelial cells, red), anti-Spike (detecting
992 SARS-CoV-2, green), and stained with Hoescht (nuclei, blue). Bottom panels show higher
993 magnification of (a) $CD68^+$ $Spike^+$ macrophage; (b) $CD68^+$ macrophage with $cytokeratin18^+$
994 content and Spike labeling in the cytosol. Yellow arrows: $cytokeratin18^+$ cells; Yellow arrowheads:
995 $CD68^+$ cells. Tissues were scanned by wide-field epifluorescence imaging. Scale bar: 50 µm; scale
996 bar for inset: 10 µm.

997 **(C)** PtdSer exposure on the surface of Calu-3 and Vero CCL81 cells in response to UV irradiation
998 or infection with SARS-CoV-2 (Cov2) for 48h, assessed by annexin V binding (percentage of
999 annexin V^+ cells) and flow cytometric analysis. The gating strategy is shown in Figure S1B.

1000 **(D)** Flow cytometric analysis of caspase-3 cleavage (Cl-caspase-3) in Calu-3 cells unstimulated
1001 (Cntrl) or infected with SARS-CoV-2 (CoV2) for 48h. The pan-caspase inhibitor z-VAD-FMK
1002 (zVAD; 20 µM) or vehicle (DMSO) were added to cell cultures after viral adsorption.
1003 Representative histogram, geometric mean fluorescence intensity (MFI), and frequency of Cl-
1004 caspase-3^+ cells (gated on Total cells/Single cells) are shown. The black line on the histogram
1005 represents the control sample labeled with secondary antibody only.

1006 **(E)** Quantification by $TCID_{50}$ of SARS-CoV-2 viral loads in Vero CCL81 infected cells. Cells
1007 were collected 48h post-infection, and viral loads were estimated for normalized amounts (10^6
1008 cells) of pre-sorted (Total cells) or Annexin V^+ (Ann^+ cells) and Annexin V^- (Ann^- cells) cells
1009 isolated by magnetic separation.

1010 **(F)** Uptake of apoptotic Vero CCL81 cells (labeled with CTFR) in response to UV irradiation
1011 (UV-AC) or infection with SARS-CoV-2 for 48h (Cov2-AC) by human monocyte-derived
1012 macrophages (labeled with CTV). Macrophages were co-incubated with AC for 2h, and

1013 internalization was assessed by flow cytometry. Representative plot and percentage of engulfment
1014 (gated on Total cells/Single cells/Live cells/CTV$^+$ cells; gating strategy in Figure S1D) are shown.
1015 **(G)** Representative maximal projection of scanning confocal images showing the uptake of UV-
1016 AC or CoV2-AC (from Vero CCL81 cells, CFSE-labelled, green) by human monocyte-derived
1017 macrophages after 2h of co-incubation. Samples were stained with Hoescht (nuclei, blue) and were
1018 immunolabelled with anti-Spike (SARS-CoV-2, red) and anti-CD11b (macrophage, white). Scale
1019 bar: 5 µm.
1020 Boxes represent the mean of three (C, E) or five (D, F) biological replicates, and error bars are ±
1021 S.E.M. Each biological replicate is shown as a circle. Significance was calculated by Student's test
1022 (C) or ANOVA (D, E). *, $p<0.05$ comparing the indicated groups; ns: non-significant. Data shown
1023 are from one representative out of two experiments performed independently with similar results.
1024
1025 **Figure. 2. Engulfment of SARS-CoV-2-infected dying cells impairs macrophage anti-**
1026 **inflammatory functions.**
1027 Macrophages were unstimulated (Cntrl), co-incubated with apoptotic Vero CCL81 cells (AC)
1028 isolated from UV-irradiated (UV-AC) or SARS-CoV-2-infected (CoV2-AC) cultures, stimulated
1029 with the supernatants of infected apoptotic cells (CoV2-AC Sup), or infected with CoV2 at MOI
1030 of 1 (CoV2), as indicated.
1031 **(A)** Heatmap showing the expression of M2-marker genes (*CCL18*, *MRC1*, *MMP9*, *PPARγ,* and
1032 *CD163*) in human monocyte-derived macrophages 24h after stimulation, calculated as log2 fold
1033 change relative to Cntrl. mRNA expression was determined by RT-qPCR and normalized to
1034 *GAPDH*. Data represent the mean of biological triplicates.

1035 **(B)** Flow cytometric analysis of CD206 expression on the cell surface of human monocyte-derived
1036 macrophages (gated on Total cells/Single cells/Live cells; gating strategy in Figure S2A) 24h after
1037 stimulation. Representative histograms and quantification of geometric mean fluorescence
1038 intensity (MFI) are shown. The black line on the histogram represents FMO control.
1039 **(C-D)** Flow cytometric analysis of CD206 expression on the cell surface of THP1-derived
1040 macrophages 24h after stimulation. **(C)** Where indicated, isolated CoV2-AC were UV-irradiated
1041 for 20 min prior to co-incubation to inactivate SARS-CoV-2. Quantification of CD206 MFI is
1042 shown. **(D)** The responses of macrophages to sterile UV-AC and virus-loaded CoV2-AC were
1043 compared to infection with CoV2 in the presence of UV-AC (UV-AC + CoV2). Quantification of
1044 CD206 MFI is shown.
1045 **(E)** *IL6* expression in monocyte-derived macrophages 24h after stimulation showed as fold change
1046 relative to Cntrl. mRNA expression was determined by RT-qPCR and normalized to GAPDH.
1047 **(F)** CBA quantification of IL-6 and IL-1β in the culture supernatants of the monocyte-derived
1048 macrophages 24h after stimulation.
1049 **(G)** ELISA quantification of IL-6 in the culture supernatants of THP1-derived macrophages 24h
1050 after stimulation. Where indicated, isolated CoV2-AC were UV-irradiated (UV) for 20min or fixed
1051 with 2% paraformaldehyde (Fix) for 10 min prior to co-incubation.
1052 **(H-J)** ELISA quantification of IL-6 in the culture supernatants of human monocyte-derived
1053 macrophages 24h after stimulation. **(H)** IL-6 secretion in response to CoV2-AC was compared to
1054 apoptotic cells isolated from Vero CCL81 cells similarly infected with Coxsackievirus (Coxsackie-
1055 AC). **(I)** PtdSer on the surface of CoV2-AC was blocked by incubation with Annexin V (Ann, 0.1
1056 μg/mL) prior to addition to macrophage cultures (supplemented with Ca^{+2}) to inhibit AC binding.

1057 **(J)** CoV2-AC and macrophages were co-incubated in the presence of Cytochalasin D (Cyto D, 10
1058 μM) to inhibit AC internalization.
1059 Boxes represent the mean of three biological replicates using cells from a single donor (B, E, F, I,
1060 and J), two donors (H), or THP-1-derived cells (C, G, H). Error bars are ± S.E.M. Each biological
1061 replicate is shown as a circle. Significance was calculated by ANOVA. *, $p<0.05$ comparing the
1062 indicated groups; ns: non-significant. Data shown are from one representative out of at least two
1063 experiments performed independently with similar results.
1064
1065 **Figure 3. Engulfment of SARS-CoV-2-infected dying cells suppresses continual efferocytosis**
1066 **by macrophages**
1067 (**A**) Expression of efferocytic receptors in human monocyte-derived macrophages. Macrophages
1068 were unstimulated (Cntrl), co-incubated for 24h with apoptotic Vero CCL81 cells (AC) isolated
1069 from UV-irradiated (UV-AC) or SARS-CoV-2-infected (CoV2-AC) cultures, or infected with
1070 CoV2 at MOI of 1 (CoV2), as indicated. Expression of *CD36*, *SRA-I*, *ITGB5*, *TIMD4*, and *MERTK*
1071 are showed as fold change relative to Cntrl. mRNA levels were determined by RT-qPCR and
1072 normalized to *GAPDH*.
1073 **(B-D)** Flow cytometric analysis of two-step efferocytosis *in vitro*. **(B)** Schematic representation of
1074 consecutive co-incubations of THP1-derived macrophages with apoptotic cells prior to the
1075 assessment of cell corpse uptake by flow cytometry. **(C)** Percentage of macrophages (CTV-
1076 labelled) with internalized UV-AC or CoV2-AC isolated from Vero CCL81 cell cultures (labeled
1077 with pHRodo), 18h after co-incubation. pHRodo$^+$ macrophages were gated on Total cells/Single
1078 cells/Live cells/CTV$^+$ (gating strategy is displayed in Figure S2L). **(D)** Macrophages were
1079 subsequently incubated with CTFR-labelled, UV-irradiated apoptotic Jurkat cells (UV-Jurkat) for

1080 2h. UV-Jurkat uptake in 2nd round of engulfment is shown as the percentage of $CTFR^+$
1081 macrophages within $PhRodo^+$ populations (gated on Total cells/Single cells/Live cells/ CTV^+/
1082 $pHRodo^+$).
1083 Boxes represent the mean of three biological replicates using cells from a single donor in (A) or
1084 THP-1-derived macrophages in quadruplicate (C and D). Error bars are ± S.E.M. Each biological
1085 replicate is shown as a circle. Significance was calculated by ANOVA (A) or Student's test (C and
1086 D). *, $p<0.05$ comparing the indicated groups; ns: non-significant. Data shown are from one
1087 representative out of two experiments performed independently with similar results.
1088
1089 **Figures 4. Lung monocytes and macrophages of severe COVID-19 patients express reduced**
1090 **levels of efferocytic receptors.**
1091 **(A-B)** Representative histological findings in post-mortem lung tissue from control tissue (Cntrl)
1092 and COVID-19 patients, obtained by ultrasound-guided minimally invasive autopsy. Tissue
1093 samples were immunolabelled with anti-S100A9 (phagocytes, green), **(A)** anti-CD36 (red), or **(B)**
1094 anti-MERTK (red) and stained with DAPI (nuclei, blue). Representative images show cropped
1095 details of lung tissues scanned by wide-field epifluorescence imaging. Scale bar: 10 µm. The mean
1096 fluorescence intensity (MFI) of CD36 and MERTK of at least 200 $S1009^+$ cells are shown (n = 3
1097 individuals per group).
1098 **(C)** GSEA analysis for efferocytosis-related gene sets in early-infiltrating phagocytes ($S1009^+$
1099 $CCL18^-$) and in anti-inflammatory monocytes-derived macrophages ($CD14^+$ $S11009^-$ $CCL18^+$)
1100 clusters from the bronchoalveolar lavage of mild (M) and severe (S) COVID-19 patients versus
1101 healthy individuals. The corrplot depicts the normalized enrichment score (NES), and p value for
1102 the gene sets indicated on the y axis.

1103 **(D)** Enriched efferocytosis-related Gene Ontology (GO) terms in genes repressed in virus-positive
1104 alveolar macrophages versus virus-negative cells.
1105 **(E)** mRNA expression of efferocytic receptors *CD36*, *SRA-I*, *ITGB5*, *TIMD4*, and *MERTK* in
1106 PMBC isolated from the blood of healthy donors (HC, n=25) or patients with COVID-19 (n=42).
1107 mRNA levels were determined by RT-qPCR and normalized to *GAPDH*.
1108 **(F)** mRNA expression of efferocytic receptors *CD36*, *SRA-I*, *ITGB5*, *TIMD4*, and *MERTK* in
1109 PMBC isolated from the blood of healthy donors (HC, n=13) or patients with acute respiratory
1110 distress syndrome unrelated to COVID-19 (non-COVID-19 ARDS, n=13). mRNA levels were
1111 determined by RT-qPCR and normalized to *GAPDH*.
1112 **(G)** Stratification of *CD36*, *SRA-1*, and *TIMD4* expression according to COVID-19 patients'
1113 hyperinflammation score (cHIS) (n=42).
1114 **(H)** Representative maximal projection of scanning confocal images showing the uptake of AC by
1115 monocytes from healthy donors (HC, n=25) and COVID-19 patients (n=16) after 2h of co-
1116 incubation. Actin filaments (F-actin) were stained with phalloidin (AF-488, green), and the nuclei
1117 were stained with Hoescht (blue). White arrows indicate transient reorganization of actin filament
1118 upon engulfment. Scale bar: 5 µm. The uptake of AC by the monocytes was assessed and
1119 associated with the cHIS score of the patients.
1120 Dots represent an $S1009^{+}$ cell (A and B) or data from each donor (E-H), the crossing line represents
1121 the mean, and error bars are ± S.E.M. Significance was calculated by Mann-Whitney test (A and
1122 B, E-F) or ANOVA (G and H). *, $p<0.05$ comparing the indicated groups; ns: non-significant.
1123
1124
1125 **Supporting information captions**

1126

1127 **Figure S1. SARS-CoV-2 -apoptotic cells are engulfed by macrophages**

1128 **(A)** Representative histological findings in post-mortem lung tissue from COVID-19 patients,
1129 obtained by ultrasound-guided minimally invasive autopsy. Representative differential
1130 interference contrast (upper panel) and immunofluorescence (middle panel) images of tissue from
1131 P2 patient immunolabelled with anti-cleaved caspase 3 (red), anti-dsRNA (SARS-CoV2, green),
1132 and stained with DAPI (nuclei, blue) for the detection of caspase-3 activation in infected cells. The
1133 bottom panels show higher magnification of the three selected areas. Arrows indicate cells positive
1134 for both Cl-caspase-3 and dsRNA (white arrows: type II pneumocytes; white arrowheads: type I
1135 pneumocytes; *cleaved-Casp3^{+} non-epithelial cell). Tissues were scanned by wide-field
1136 epifluorescence imaging. Scale bar: 100 µm (upper and middle panels) or 50 µm (selected areas).

1137 **(B)** Representative gating strategy used to determine the PtdSer exposure on the surface of Calu-
1138 3 and Vero CCL81 cells in response to UV irradiation or infection with SARS-CoV-2 (Cov2) for
1139 48h, assessed by annexin V binding and flow cytometric analysis (related to Figure 1C)

1140 **(C)** $TCID_{50}$ quantification of SARS-CoV-2 viral loads from detached, apoptotic Calu-3 and Vero
1141 CCL81 cells (CoV2-AC, 10^6 cells) and their cell-free supernatants, collected 48h post-infection
1142 and isolated as described in the Methods.

1143 **(D)** Uptake of apoptotic Calu-3 and Vero CCL81 cells (labeled with CFSE) in response to UV
1144 irradiation (UV-AC) or infection with SARS-CoV-2 for 48h (Cov2-AC) by THP-1-derived
1145 macrophages (labeled with CTFR). Macrophages were co-incubated with AC for 2h, and
1146 internalization was assessed by flow cytometry. Representative gating strategy, plots, and
1147 percentage of engulfment (gated on Total cells/Single cells/Live cells/CTFR^{+} cells) are shown.

1148 **(E)** Human monocyte-derived macrophages or THP-1-derived macrophages were unstimulated
1149 (Cntrl), co-incubated with apoptotic Vero CCL81 cells isolated from UV-irradiated (UV-AC) or
1150 SARS-CoV-2-infected (CoV2-AC) cultures, stimulated with the supernatants of infected apoptotic
1151 cells (CoV2-AC Sup), or infected with SARS-CoV-2 at MOI of 1 (CoV2), as indicated. The
1152 percentage of cellular viability was measured using a viability probe 24h post-stimulation and
1153 analysis by flow cytometry (gated on Total cells/Single cells).
1154 Boxes represent the mean of three biological replicates, and error bars are ± S.E.M. Each biological
1155 replicate is shown as a circle. Significance was calculated by Student's test (C-D) or ANOVA (E).
1156 *, $p<0.05$ comparing the indicated groups; ns: non-significant. Data shown are from one
1157 representative out of two experiments performed independently with similar results.
1158
1159 **Figure S2. Engulfment of SARS-CoV-2-infected dying cells switches macrophage phenotype**
1160 **in response to efferocytosis.**
1161 **(A)** Representative gating strategy used to determine the CD206 expression on the surface of
1162 macrophages in response to the different stimulus by flow cytometry (backgating corresponds to
1163 FMO control showed in Fig. 2B)
1164 **(B)** THP-1-derived macrophages were unstimulated (Cntrl), co-incubated with UV-AC, CoV2-
1165 AC, or CoV2-AC Sup obtained from Vero CCL81 cells, or infected with CoV2, as indicated.
1166 Expression of *MRC1* in macrophages showed as fold change relative to Cntrl was assessed 24h
1167 after stimulation. mRNA expression was determined by RT-qPCR and normalized to *GAPDH*.
1168 **(C-D)** THP-1-derived macrophages were incubated with UV-AC, Cov2-C, or CoV2-Sup obtained
1169 from Calu-3 **(C)** or Vero CCL81 **(D)** infected cell cultures. CD206 expression on the cell surface
1170 24h after stimulation was assessed by flow cytometry (gated on Total cells/Single cells/Live cells).

1171 Representative histograms and quantification of geometric mean fluorescence intensity (MFI) of
1172 CD206 are shown.
1173 **(E)** Quantification by $TCID_{50}$ of the SARS-CoV-2 viral loads in 10^6 AC isolated from Vero CCL81
1174 infected cells, either intact (CoV2-AC) or UV-irradiated for 20 min for viral inactivation (CoV2-
1175 AC UV).
1176 **(F)** THP-1-derived macrophages were incubated with UV-AC, Cov2-AC, or CoV2-Sup obtained
1177 from infected Vero CCL81 cells or infected with Cov2. Expression of *MRC1* in macrophages
1178 showed as fold change relative to Cntrl was assessed 24h after stimulation. mRNA expression was
1179 determined by RT-qPCR and normalized to *GAPDH*.
1180 **(G-H)** THP-1-derived macrophages were incubated for 24h with UV-AC, Cov2-C, or CoV2-Sup
1181 obtained from Calu-3 or Vero CCL81 infected cell cultures, as indicated. IL-6 **(G)** and IL-1β **(H)**
1182 in the culture supernatants were quantified by CBA.
1183 **(I)** Quantification by $TCID_{50}$ of the viral loads in 10^6 AC isolated from Vero CCL81 cells similarly
1184 infected with either Coxsackie virus (Coxsackie-AC) or SARS-CoV-2 (CoV2-AC).
1185 **(J)** ELISA quantification of IL-6 in the culture supernatants of THP-1-derived macrophages
1186 stimulated with Cov2-AC for 24h. PtdSer on the cell surface was blocked to inhibit AC binding
1187 by incubation of CoV2-AC with Annexin V (Ann, 0.01 and 0.1 μg/mL) prior to addition to
1188 macrophage cultures.
1189 **(K)** THP-1-derived macrophages were incubated with UV-AC or Cov2-AC obtained from infected
1190 Vero CCL81 cells or infected with CoV2. Expression of the efferocytic receptors *CD36*, *SRA-I*,
1191 *ITGB5*, *TIMD4*, and *MERTK* showed as fold change relative to Cntrl was assessed 24h after
1192 stimulation. mRNA levels were determined by RT-qPCR and normalized to *GAPDH*.

1193 **(L)** Representative gating strategy used to determine CTV-labelled macrophage populations for
1194 the two-step efferocytosis experiment showed in Figures 3C and D.
1195 **(M)** THP-1-derived macrophages (CTV-labelled) were infected or not with SARS-CoV-2 (CoV2)
1196 at MOI of 1 for 18h and subsequently were incubated with CTFR-labelled, UV-irradiated apoptotic
1197 Jurkat cells (UV-Jurkat) for 2h. UV-Jurkat uptake is shown as the percentage of $CTFR^+$ (gated on
1198 Total cells/Single cells/Live cells/ CTV^+).
1199 Boxes represent the mean of three biological replicates, and error bars are ± S.E.M. Each biological
1200 replicate is shown as a circle. Significance was calculated by ANOVA (B-D, F-H, and J-K) or
1201 Student's test (I and M). *, $p<0.05$ comparing the indicated groups; ns: non-significant. Data
1202 shown are from one representative out of two experiments performed independently with similar
1203 results.
1204
1205 **Figure S3. Analysis of cytokine production and monocyte subpopulations in COVID-19**
1206 **patients.**
1207 **(A)** CBA quantification of IL-6, IL-8, IL-10, IL-1β, TNF-α, and IL-12 in the plasma from healthy
1208 donors (HC, n=19) and COVID-19 patients (n=28).
1209 **(B)** Representative gating strategy used to determine the percentage of classical, intermediate, non-
1210 classical monocyte subpopulations, CD36, and HLA-DR expression on the surface of blood
1211 monocytes from HC and COVID-19 patients (related to Figs. S3 C-I). Displayed plots correspond
1212 to CD36-PE FMO control.
1213 **(C-D)** The frequency **(C)** and absolute number **(D)** of $CD14^+$ blood monocytes from HC (n=22)
1214 and COVID-19 patients (n=26) were determined by flow cytometry (gated on Total cells/Single
1215 cells/Live cells/Lin^-).

1216 **(E)** Percentage of HLA-DR^{+} monocytes in blood from healthy donors (HC, n=22) and COVID-19
1217 patients (n=26), determined by flow cytometry (gated on Total cells/Single cells/Live cells/Lin^{-}
1218 /CD14^{+}).
1219 **(F-H)** Frequency of **(F)** classical CD14^{+}CD16^{-}, **(G)** intermediate CD14^{hi}CD16^{+} and **(H)** non-
1220 classical CD14^{int}CD16^{+} monocytes in blood samples from healthy donors (HC, n=22) and
1221 COVID-19 patients (n=26) are shown (gated on Total cells/Single cells/Live cells/Lin^{-} CD14^{+}).
1222 **(I)** Representative plots, frequency, and MFI of CD36 expression in CD14^{hi} monocytes from HC
1223 and COVID-19 patients (gated on Total cells/Single cells/Live cells/Lin^{-} CD14^{hi}).
1224 **(J)** The uptake of zymosan particles (labeled with Texas-Red) by monocytes from healthy donors
1225 (HC, n=7) and COVID-19 patients (n=7) was determined by epifluorescence microscopy. Each
1226 dot represents the data from each donor, the crossing line represents mean, and error bars ± S.E.M.
1227 Significance was calculated by the Mann-Whitney test (A and C-I) or Student's test (J). *, $p<0.05$
1228 comparing the indicated groups; ns: non-significant.
1229
1230 **Table S1.** Custom gene sets incorporating associated to efferocytic pathway and related to human
1231 diseases (related to Figure 4C).
1232
1233 **Table S2.** Medical characteristics of COVID-19 patients.
1234
1235 **Table S3.** Medical characteristics of nonCOVID-19 ARDS patients.
1236

A

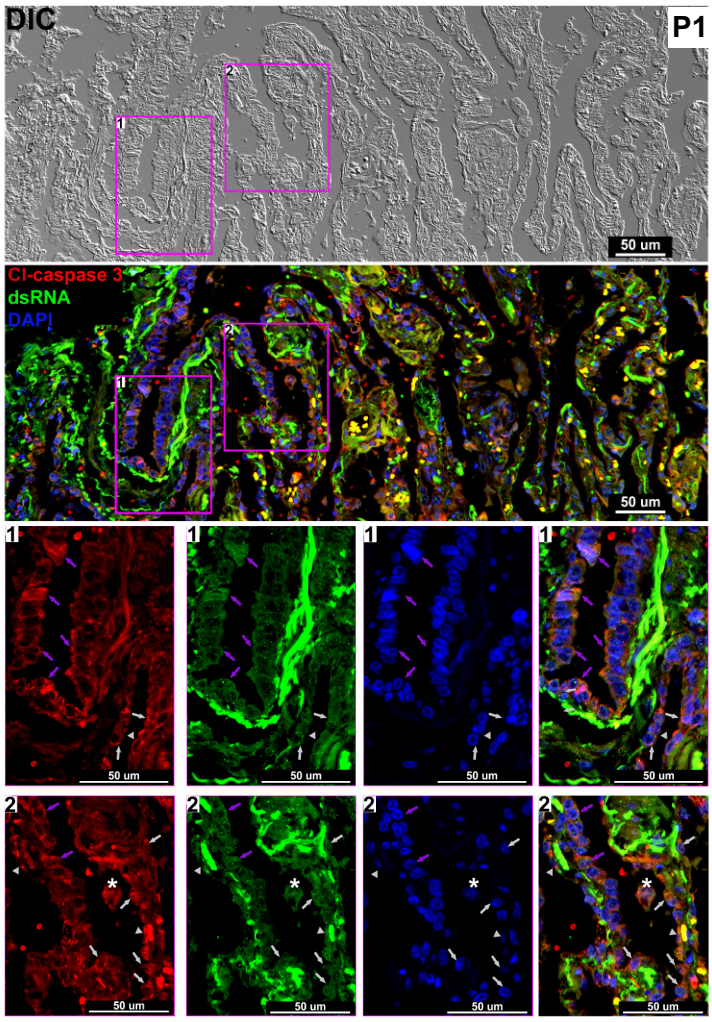
DIC
P1
50 um
Cl-caspase 3
dsRNA
DAPI

B

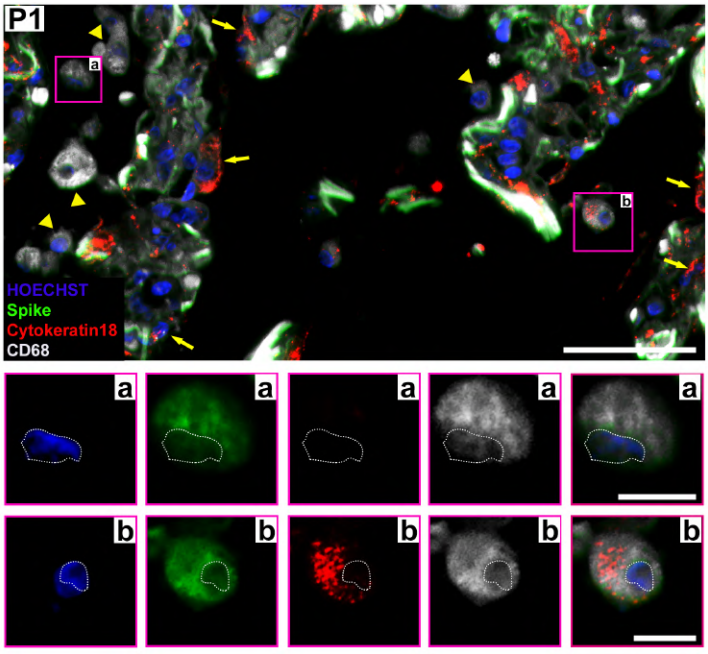
P1
HOECHST
Spike
Cytokeratin18
CD68

C

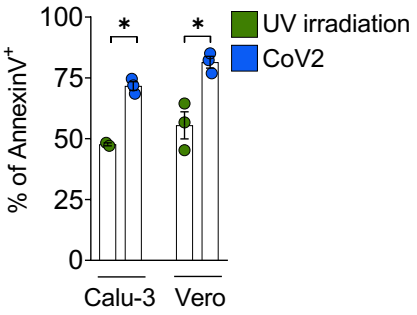
% of AnnexinV+
UV irradiation
CoV2
Calu-3
Vero

D

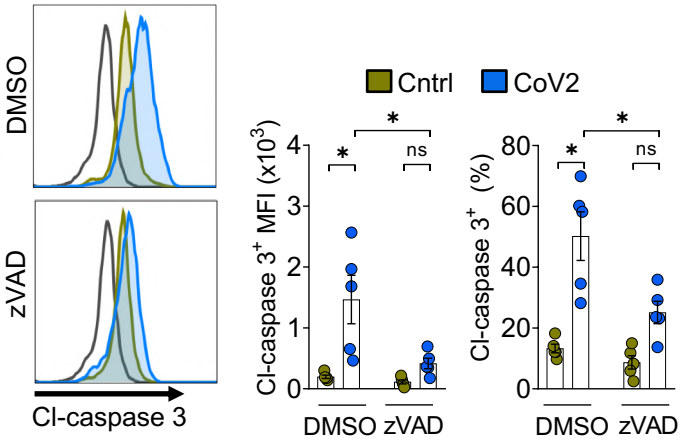
DMSO
zVAD
Cl-caspase 3
Cntrl
CoV2
Cl-caspase 3+ MFI (x10^3)
Cl-caspase 3+ (%)
ns
DMSO
zVAD

E

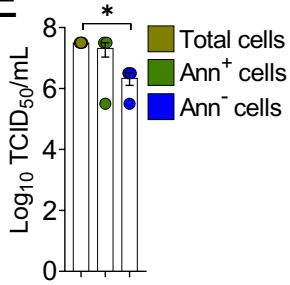
Log10 TCID50/mL
Total cells
Ann+ cells
Ann- cells

F

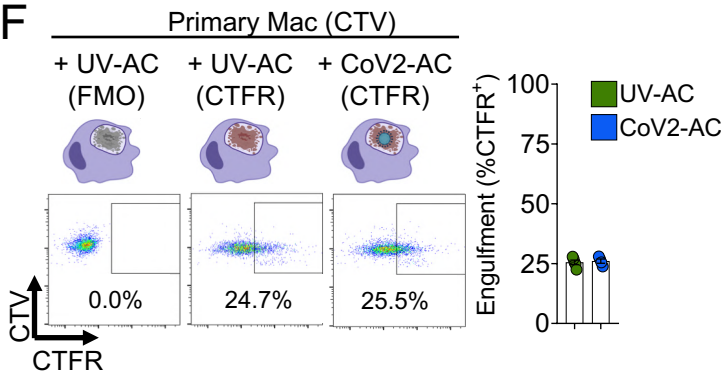
Primary Mac (CTV)
+ UV-AC (FMO)
+ UV-AC (CTFR)
+ CoV2-AC (CTFR)
0.0%
24.7%
25.5%
CTV
CTFR
Engulfment (%CTFR+)
UV-AC
CoV2-AC

G

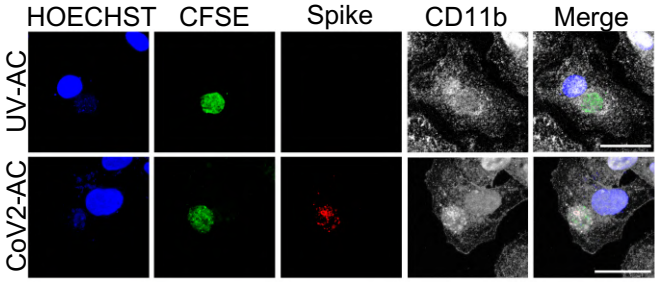
HOECHST
CFSE
Spike
CD11b
Merge
UV-AC
CoV2-AC

A
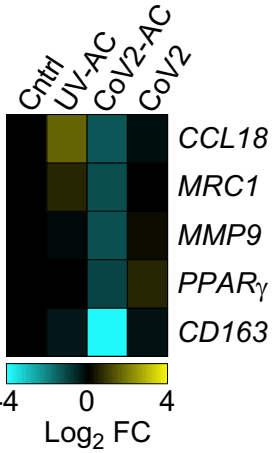
Cntrl
UV-AC
CoV2-AC
CoV2
CCL18
MRC1
MMP9
PPARγ
CD163
-4
0
4
Log2 FC

B
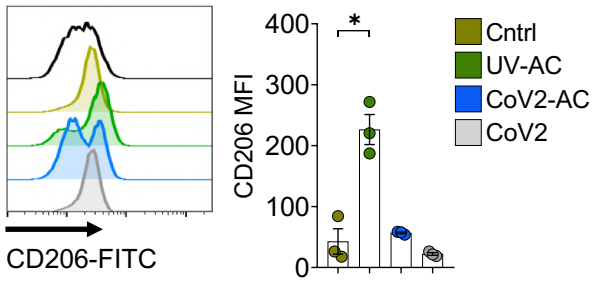
CD206-FITC
CD206 MFI
400
300
200
100
0
*
Cntrl
UV-AC
CoV2-AC
CoV2

C
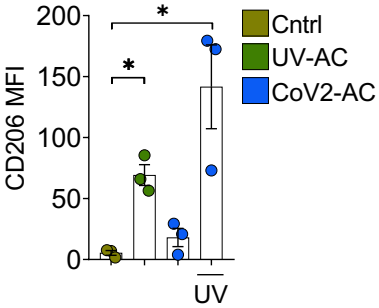
CD206 MFI
200
150
100
50
0
*
*
UV
Cntrl
UV-AC
CoV2-AC

D
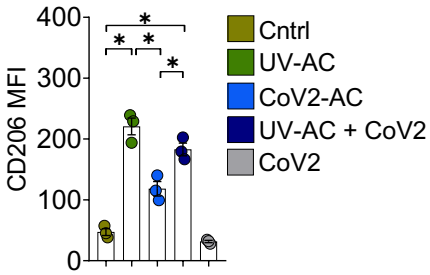
CD206 MFI
400
300
200
100
0
*
*
*
*
Cntrl
UV-AC
CoV2-AC
UV-AC + CoV2
CoV2

E
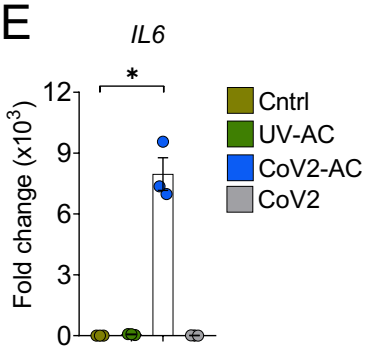
IL6
Fold change (x10³)
12
9
6
3
0
*
Cntrl
UV-AC
CoV2-AC
CoV2

F
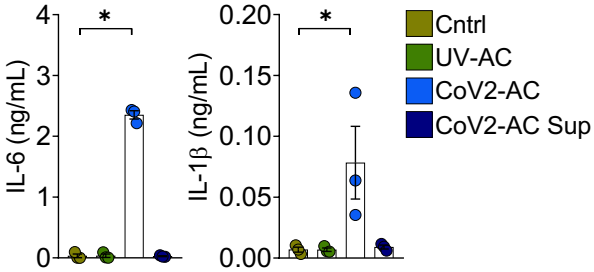
IL-6 (ng/mL)
4
3
2
1
0
*
IL-1β (ng/mL)
0.20
0.15
0.10
0.05
0.00
*
Cntrl
UV-AC
CoV2-AC
CoV2-AC Sup

G
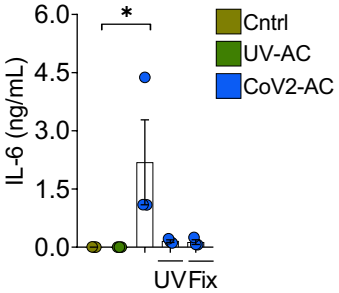
IL-6 (ng/mL)
6.0
4.5
3.0
1.5
0.0
*
UV
Fix
Cntrl
UV-AC
CoV2-AC

H
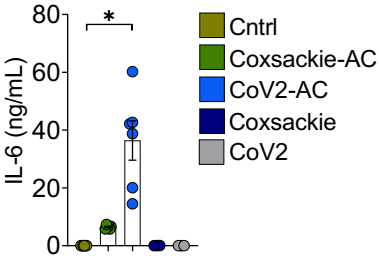
IL-6 (ng/mL)
80
60
40
20
0
*
Cntrl
Coxsackie-AC
CoV2-AC
Coxsackie
CoV2

I
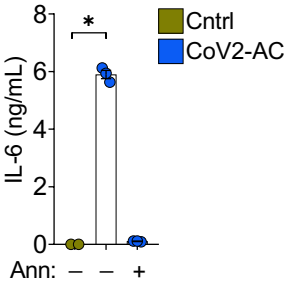
IL-6 (ng/mL)
8
6
4
2
0
*
Ann: – – +
Cntrl
CoV2-AC

J
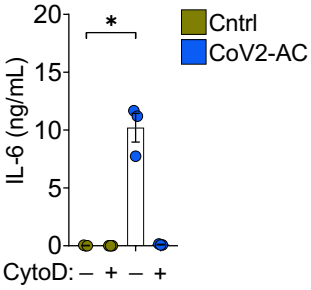
IL-6 (ng/mL)
20
15
10
5
0
*
CytoD: – + – +
Cntrl
CoV2-AC

A

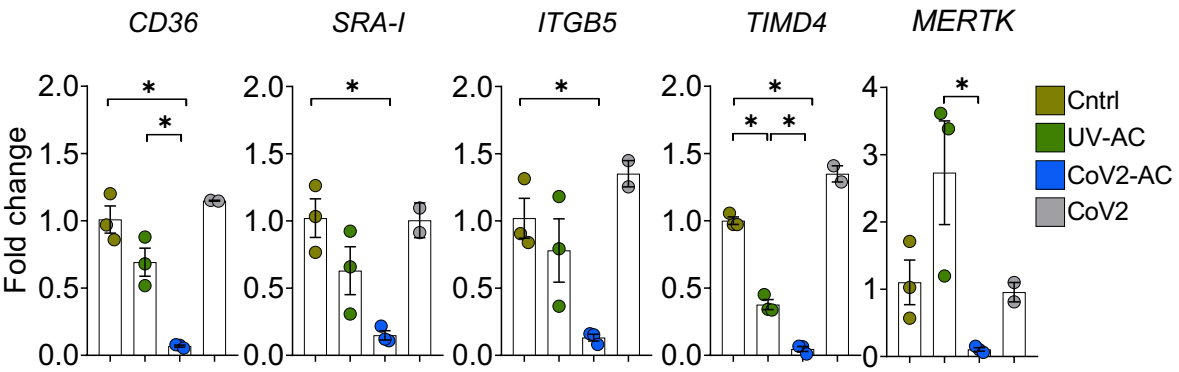
CD36
SRA-I
ITGB5
TIMD4
MERTK
Fold change
Cntrl
UV-AC
CoV2-AC
CoV2

B

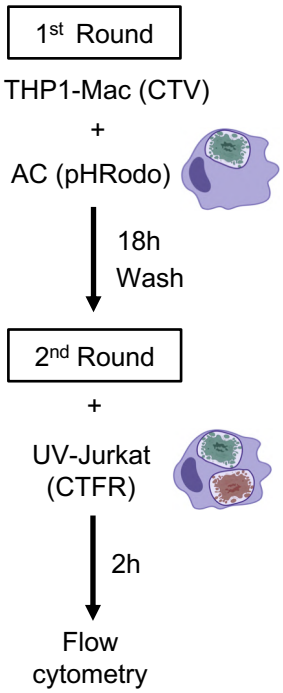
1st Round
THP1-Mac (CTV)
+
AC (pHRodo)
18h
Wash
2nd Round
+
UV-Jurkat
(CTFR)
2h
Flow
cytometry

C

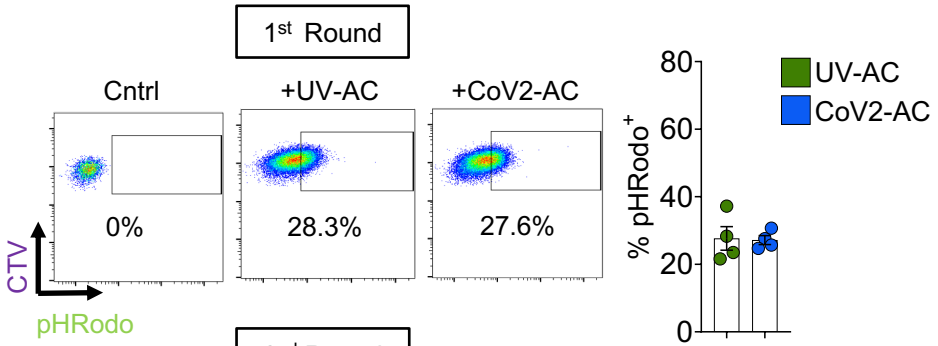
1st Round
Cntrl
+UV-AC
+CoV2-AC
0%
28.3%
27.6%
CTV
pHRodo
% pHRodo+
UV-AC
CoV2-AC

D

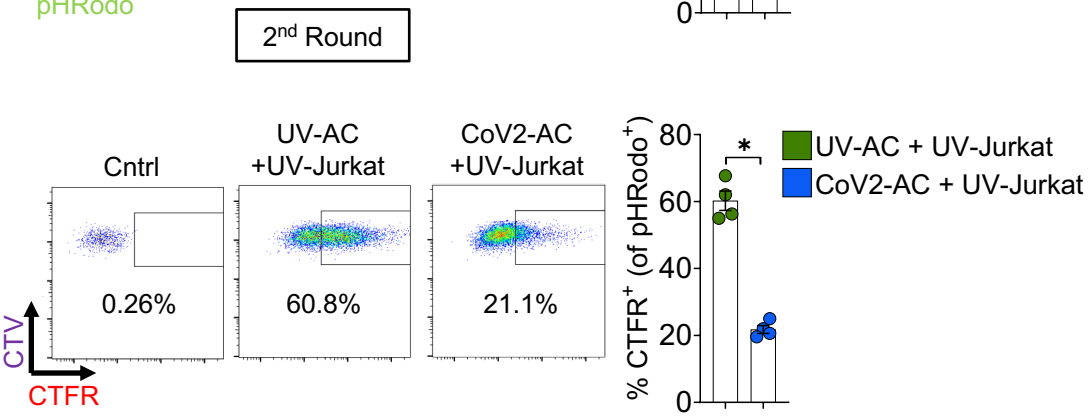
2nd Round
Cntrl
UV-AC
+UV-Jurkat
CoV2-AC
+UV-Jurkat
0.26%
60.8%
21.1%
CTV
CTFR
% CTFR+ (of pHRodo+)
UV-AC + UV-Jurkat
CoV2-AC + UV-Jurkat

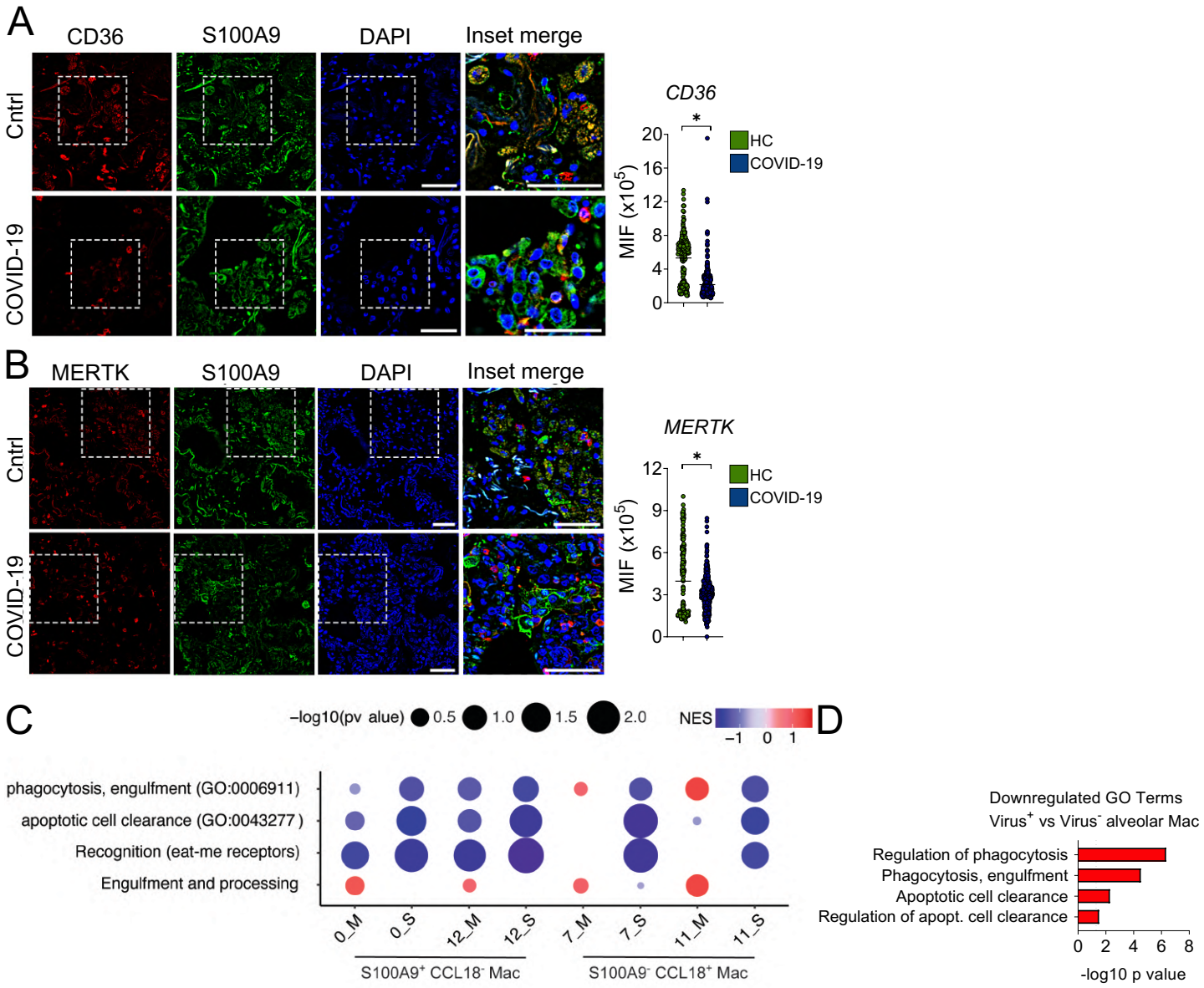
A
CD36
S100A9
DAPI
Inset merge
Cntrl
COVID-19
CD36
MIF (x10^5)
HC
COVID-19
B
MERTK
S100A9
DAPI
Inset merge
Cntrl
COVID-19
MERTK
MIF (x10^5)
HC
COVID-19
C
–log10(pv alue)
0.5
1.0
1.5
2.0
NES
–1
0
1
D
phagocytosis, engulfment (GO:0006911)
apoptotic cell clearance (GO:0043277)
Recognition (eat-me receptors)
Engulfment and processing
0_M
0_S
12_M
12_S
7_M
7_S
11_M
11_S
S100A9+ CCL18- Mac
S100A9- CCL18+ Mac
Downregulated GO Terms
Virus+ vs Virus- alveolar Mac
Regulation of phagocytosis
Phagocytosis, engulfment
Apoptotic cell clearance
Regulation of apopt. cell clearance
-log10 p value

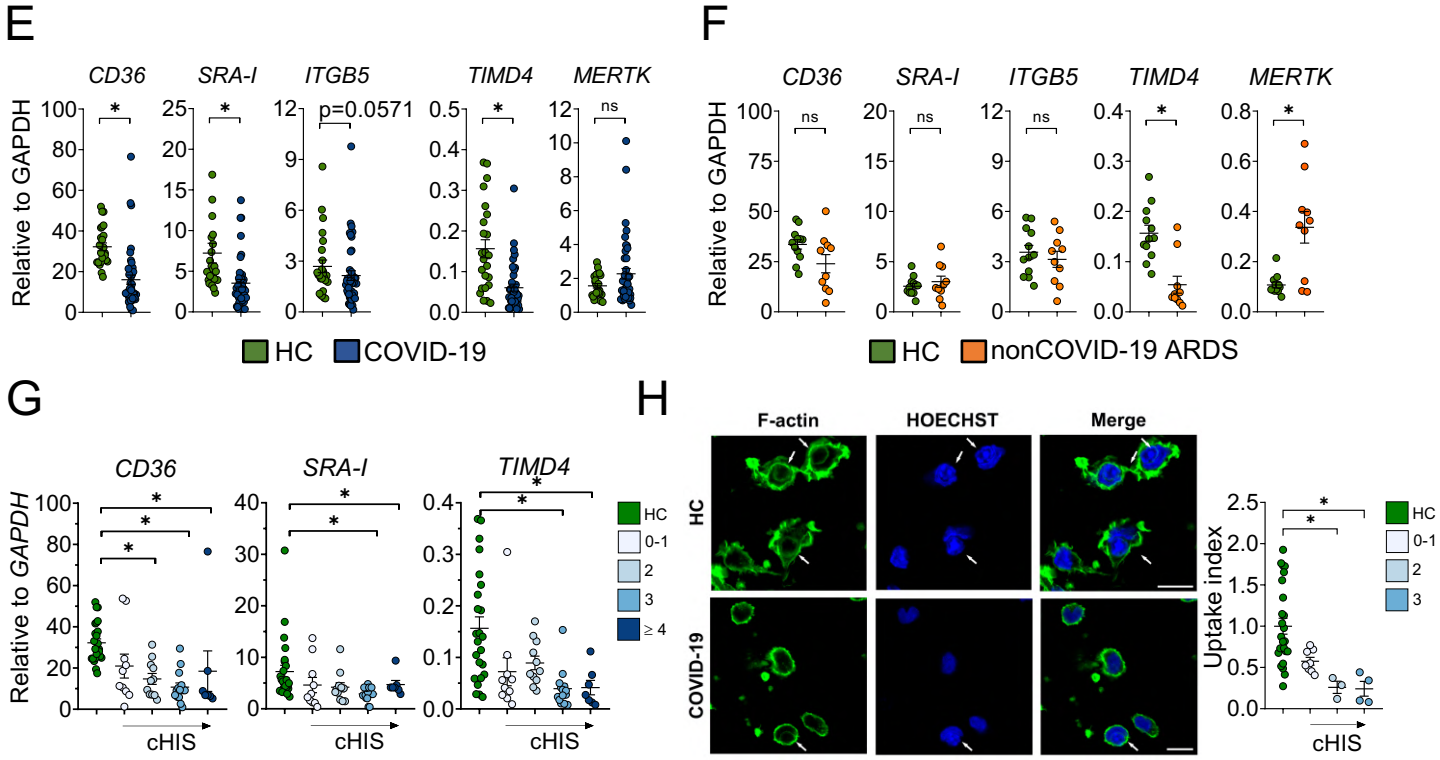
E
CD36
SRA-I
ITGB5
TIMD4
MERTK
Relative to GAPDH
p=0.0571
ns
HC
COVID-19
F
CD36
SRA-I
ITGB5
TIMD4
MERTK
Relative to GAPDH
ns
HC
nonCOVID-19 ARDS
G
CD36
SRA-I
TIMD4
Relative to GAPDH
cHIS
HC
0-1
2
3
≥ 4
H
F-actin
HOECHST
Merge
HC
COVID-19
Uptake index
cHIS
HC
0-1
2
3

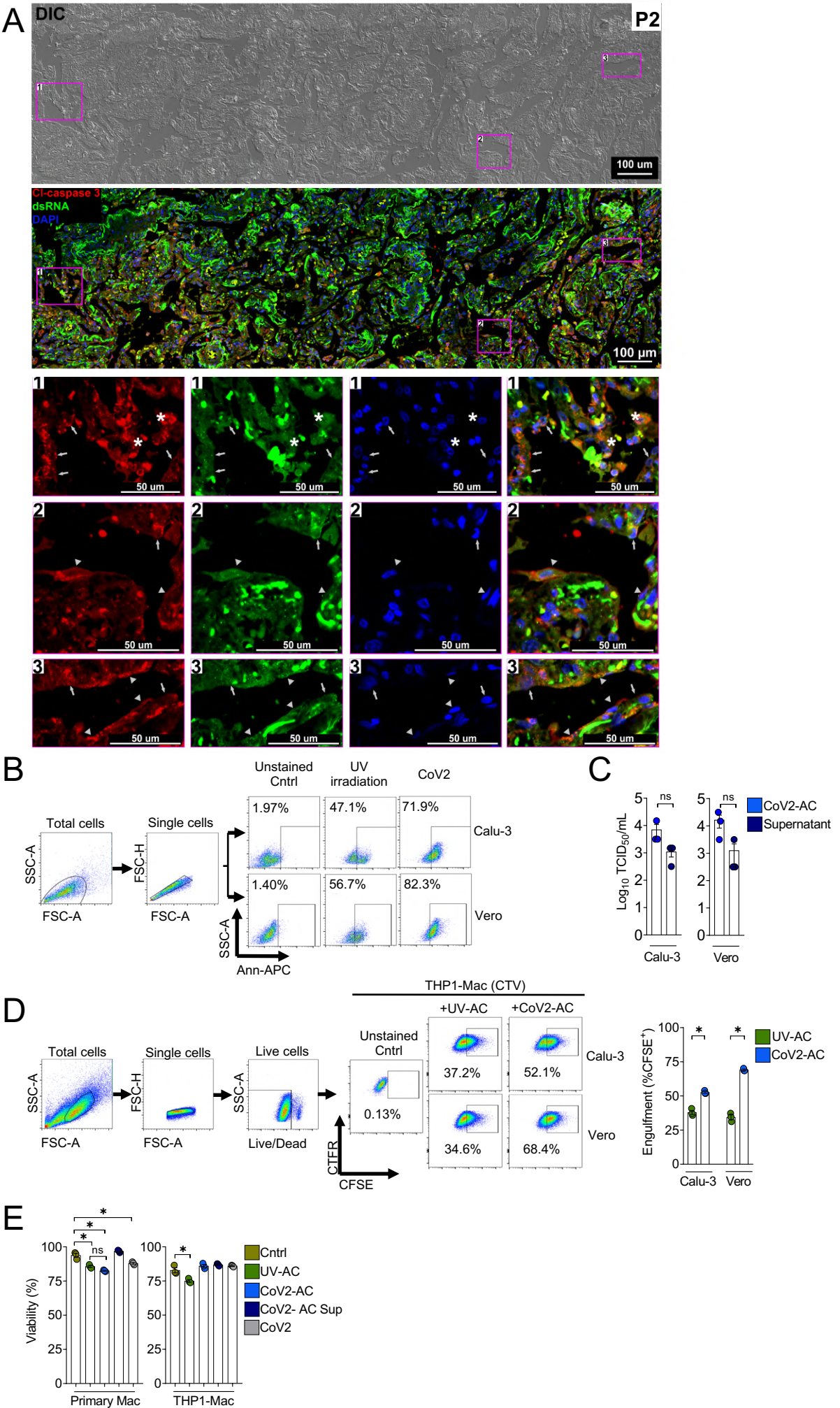
A
DIC
P2
100 um
Cl-caspase 3
dsRNA
DAPI
100 µm
50 um
B
Unstained Cntrl
UV irradiation
CoV2
Total cells
Single cells
SSC-A
FSC-A
FSC-H
1.97%
47.1%
71.9%
Calu-3
1.40%
56.7%
82.3%
Vero
Ann-APC
C
ns
CoV2-AC
Supernatant
Log10 TCID50/mL
Calu-3
Vero
D
THP1-Mac (CTV)
+UV-AC
+CoV2-AC
Unstained Cntrl
Live cells
Live/Dead
0.13%
37.2%
52.1%
34.6%
68.4%
CTFR
CFSE
UV-AC
CoV2-AC
Engulfment (%CFSE+)
E
Viability (%)
Cntrl
UV-AC
CoV2-AC
CoV2- AC Sup
CoV2
Primary Mac
THP1-Mac

Supplemental Figure 2. **Salina, dos-Santos, Rodrigues *et al.***

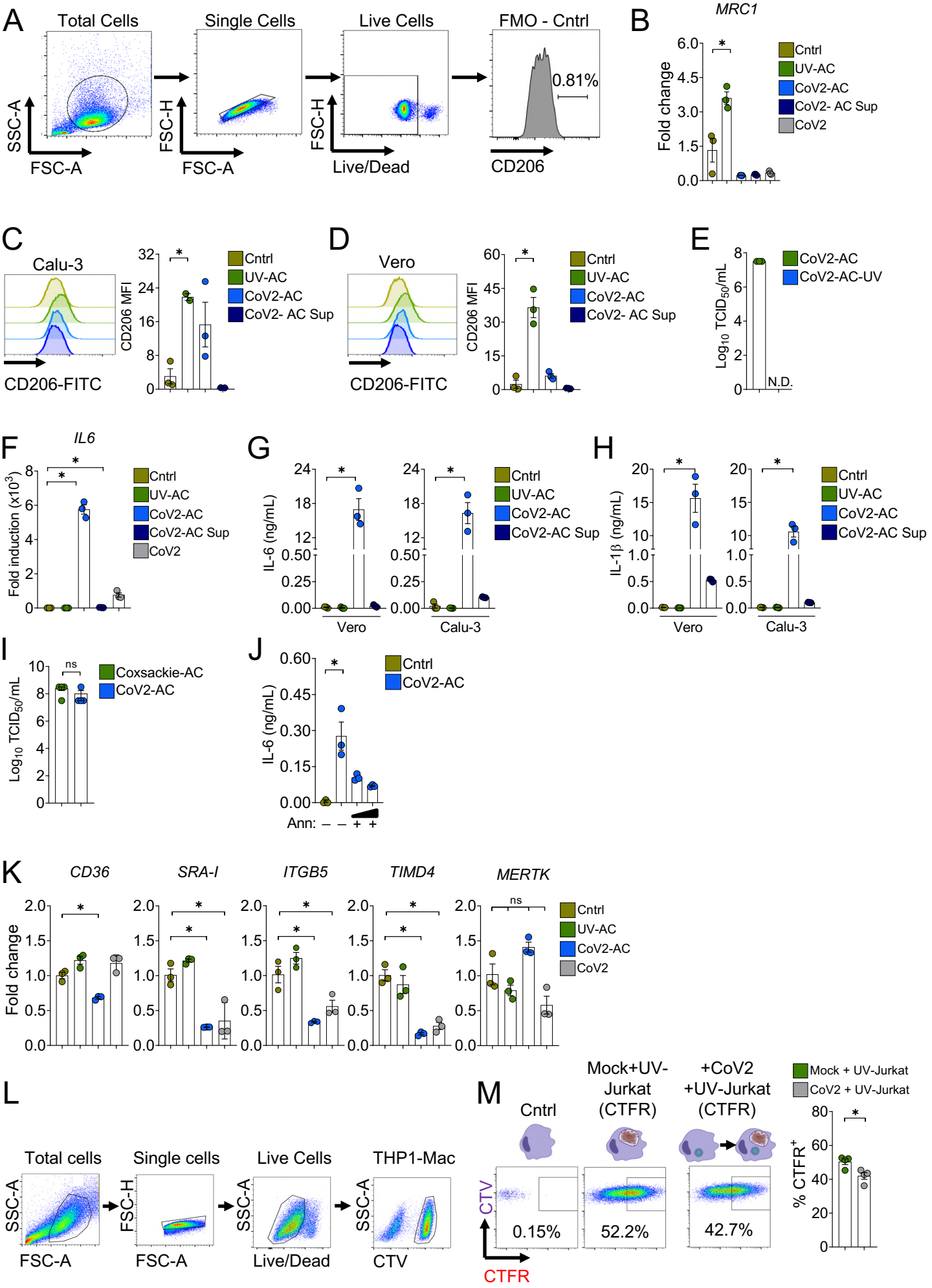

Supplemental Figure 3. **Salina, dos-Santos, Rodrigues *et al.***

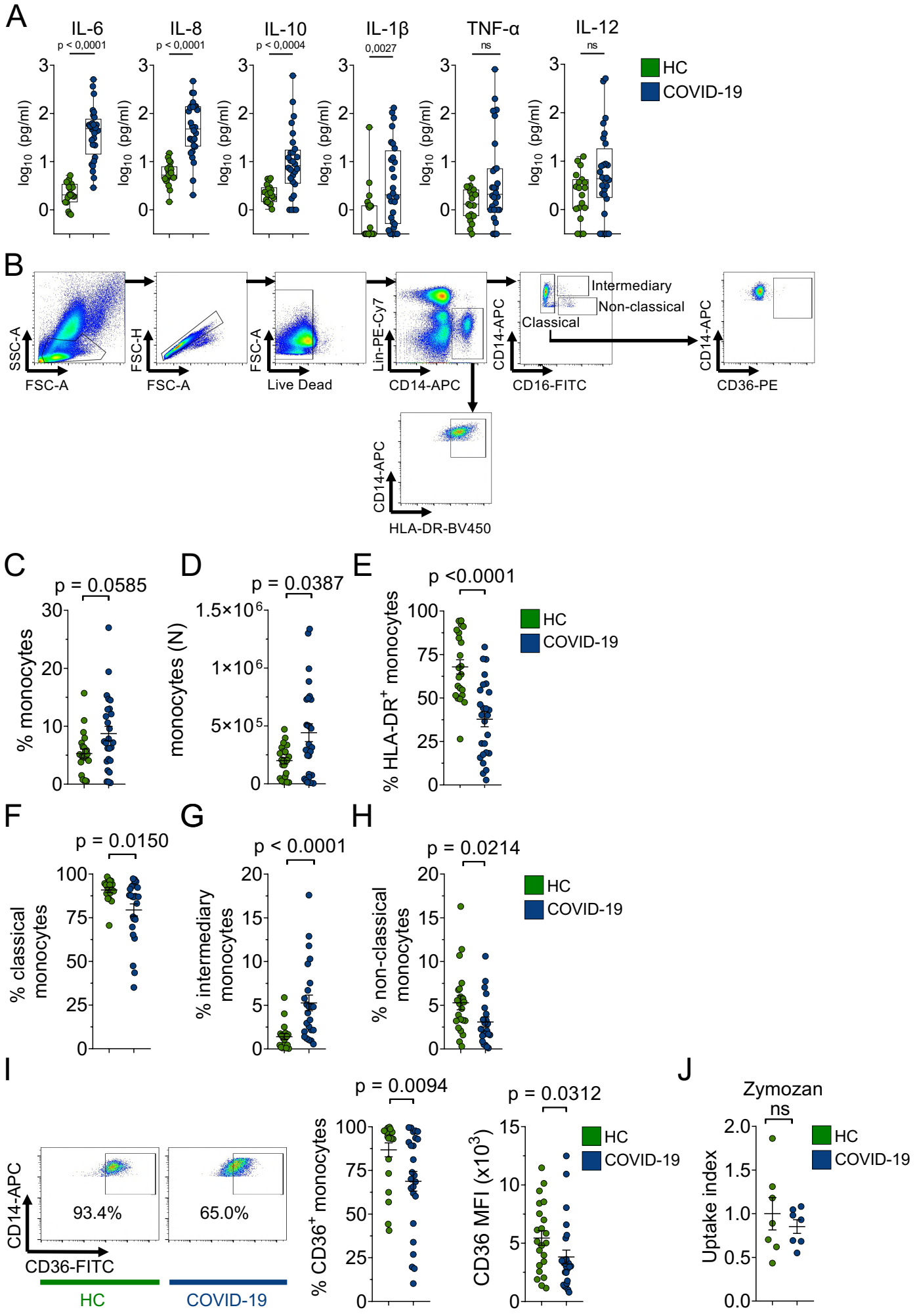

Table S1. Custom gene sets incorporating genes associated to efferocytic pathways and related to human diseases (Penberthy and Ravichandran, 2016; Boada-Romero et al., 2020) (related to Figure 4C).

Term	Gene				
Recognition (eat-me receptors)	GAS6	SCARB1	MARCO	MEGF10	STAB1
	MERTK	ITGB3	MFGE8	MSR1	STAB2
	ADGRB1	ITGAV	AXL	TIMD4	AGER
	LRP1	CD36	TYRO3	C1QA	SCARF1
Engulfment and processing	RAC2	RHOBTB1	DNM1L	ABCA1	ATG7
	RAC1	RHOG	ELMO1	RUBCN	ATG16L1
	RHOH	RAB14	SLC2A1	BECN1	GULP
	TREX1	TYROBP	SLC12A4	PIK3C3	
	RHOBTB2	DOCK1	DNASE2	ATG5	

Table S2. Medical characteristics of COVID-19 patients

	Demographics	%
Number	60	
Age	61.48 ± 16.07	
Female		43.3
	Comorbidities	
Hypertension	35	58
Obesity	32	57
Diabetes	22	37
History of smoking	8	15
Heart disease	16	27
Lung disease	11	18
Kidney disease	8	14
Cancer	6	10
History of stroke	1	2
Immunodeficiency	1	2
Autoimmune diseases	2	3
	Laboratorial findings	
CRP (mg/dL)	11.78 ± 8.09	
D-Dimers (µg/mL)	3.30 ± 3.15	
LDH (U/L)	855.39 ± 533.04	
Ferritin (ng/mL) of smoking	1494.31 ± 1374.06	
Haemoglobin (g/dL)	12.25 ± 3.35	
Neutrophils (cell/mm3)	8004.18 ± 5026.49	
Lymphocytes (cell/mm3)	1572.42 ± 1098.80	
Platelets (count/mm3)	251066.67 ± 105331.26	
	Medications	
Heparin	58	97
Antibiotics	56	93
Glucocorticoids	57	95
Oseltamivir	14	25
Antimalarial	2	4
	Respiratory status	
Mechanical ventilation	42	70
Nasal-cannula oxygen	60	100
pO2	79.87 ± 35.53	
SatO2	91.84 ± 9.90	
	Disease severity	
Mild	0	0
Moderate	10	17.24
Severe	50	86.21
	Outcome	
Death	27	46.55

*CRP: C-reactive protein (normal value <0.5 mg/dl); **D-dimers (normal value <0.5 µg/ml); :

#LDH: lactate dehydrogenase (normal range: 120–246 U/liter); [&]Ferritin (normal range: 10-291 ng/ml)

Table S3. Medical characteristics of nonCOVID-19 ARDS patients

	Demographics	%
Number	10	
Age	67.10 ± 12.04	
Female		40
	Comorbidities	
Hypertension	8	80
Obesity	4	40
Diabetes	6	60
History of smoking	7	70
Heart disease	6	60
Lung disease	5	50
Kidney disease	2	20
Cancer	2	20
History of stroke	1	10
Immunodeficiency	1	10
Autoimmune diseases	0	0
	Laboratorial findings	
CRP (mg/dL)*	8.82 ± 10.29	
D-Dimers (µg/mL)**	4.69 ± 3.69	
LDH (U/L)#	1700.22 ± 2542.49	
Ferritin (ng/mL)&	N.D.	
Haemoglobin (g/dL)	15.00 ± 4.74	
Neutrophils (cell/mm3)	9300.00 ± 4998.67	
Lymphocytes (cell/mm3	2070.00 ± 1418.18	
Platelets (count/mm3)	222300.000 ± 116946.38	
	Medications	
Heparin	9	90
Antibiotics	9	90
Glucocorticoids	6	60
Oseltamivir	1	10
Antimalarial	0	0
	Respiratory status	
Mechanical ventilation	7	70
Nasal-cannula oxygen	10	100
pO2	71.27 ± 18.18	
SatO2	91.55 ± 7.73	
	Disease severity	
Mild	0	0
Moderate	1	10
Severe	9	90
	Outcome	
Death	7	70

*CRP: C-reactive protein (normal value <0.5 mg/dl); **D-dimers (normal value <0.5 µg/ml); :

#LDH: lactate dehydrogenase (normal range: 120–246 U/liter); &Ferritin (normal range: 10-291 ng/ml)